The Astrophysical Journal, 705:1000–1018, 2009 November 1 doi:10.1088/0004-637X/705/1/1000

EFFECTS OF FOSSIL MAGNETIC FIELDS ON CONVECTIVE CORE DYNAMOS IN A-TYPE STARS

Nicholas A. Featherstone[1], Matthew K. Browning[2], Allan Sacha Brun[3], and Juri Toomre[1]
[1] JILA and Department of Astrophysical and Planetary Sciences, University of Colorado, Boulder, CO 80309-0440, USA; feathern@solarz.colorado.edu
[2] Canadian Institute for Theoretical Astrophysics, University of Toronto, Toronto, ON M5S3H8, Canada
[3] DSM/IRFU/SAp, CEA-Saclay & UMR AIM, CEA-CNRS-Université, Paris 7, 91191 Gif-sur-Yvette, France
Received 2009 May 8; accepted 2009 September 3; published 2009 October 16

ABSTRACT

The vigorous magnetic dynamo action achieved within the convective cores of A-type stars may be influenced by fossil magnetic fields within their radiative envelopes. We study such effects through three-dimensional simulations that model the inner 30% by radius of a 2 $M_\odot$ A-type star, capturing the convective core and a portion of the overlying radiative envelope within our computational domain. We employ the three-dimensional anelastic spherical harmonic code to model turbulent dynamics within a deep rotating spherical shell. The interaction between a fossil field and the core dynamo is examined by introducing a large-scale magnetic field into the radiative envelope of a mature A star dynamo simulation. We find that the inclusion of a twisted toroidal fossil field can lead to a remarkable transition in the core dynamo behavior. Namely, a super-equipartition state can be realized in which the magnetic energy built by dynamo action is 10-fold greater than the kinetic energy of the convection itself. Such strong-field states may suggest that the resulting Lorentz forces should seek to quench the flows, yet we have achieved super-equipartition dynamo action that persists for multiple diffusion times. This is achieved by the relative co-alignment of the flows and magnetic fields in much of the domain, along with some lateral displacements of the fastest flows from the strongest fields. Convection in the presence of such strong magnetic fields typically manifests as 4–6 cylindrical rolls aligned with the rotation axis, each possessing central axial flows that imbue the rolls with a helical nature. The roll system also possesses core-crossing flows that couple distant regions of the core. We find that the magnetic fields exhibit a comparable global topology with broad, continuous swathes of magnetic field linking opposite sides of the convective core. We have explored several poloidal and toroidal fossil field geometries, finding that a poloidal component is essential for a transition to super-equipartition to occur.

Key words: convection – MHD – stars: evolution – stars: interiors – stars: magnetic fields

Online-only material: color figures

1. AP STARS AND MAGNETISM

The unusual chemical abundances of peculiar A-type (Ap) stars were first noted by Maury (1897), who discovered a strong Si II doublet in the spectrum of α^2CVn. Subsequent observations of this and similar stars over the last century have shown these stars to exhibit strong and variable spectral lines (relative to solar values) in Si and certain rare earth elements (e.g., Sr, Hg, in addition to others). Most, if not all, of the Si and Sr–Cr–Eu peculiarity classes possess equally variable and unusually strong magnetic fields (Babcock 1947; Mestel 1999). Puzzlingly, only about 10% of A stars have detectable magnetic fields, the nature and source of which has been a subject of much study (Moss 2001). Whether in the Ap or A stars, magnetic fields are generally thought to be of primordial origin, resulting from the diffusive evolution of the magnetic field threading the initial molecular cloud. However, convection in the cores of these stars may also play a significant role. Our interests concern the nature of the interaction between such a primordial magnetic field and a core dynamo harbored within the convective interior of an A-type star.

1.1. Observations of Magnetic Fields

Observations of magnetic fields in Ap stars are carried out primarily through measurements of the longitudinal (line-of-sight) field, deduced by measuring the wavelength shifts between spectral lines of opposite circular polarization (Mathys 2001). Typical longitudinal field strengths for the magnetic Ap stars are a few hundred Gauss, but field strengths ranging from 20,000 G down to a lower threshold of ∼300 G have been observed (Aurière et al. 2007). Some inferences about the nature of the structure of magnetic fields on these stars have been made through complementary measurements of the magnetic field modulus (also termed "the surface field"). However, Doppler broadening makes such measurements possible only for the slowest rotators (Mathys 2001). Observations of the slow rotators suggest a lower cutoff for the mean modulus of about 3000 G, well above the detectability limit (Mathys et al. 1997; Freyhammer et al. 2008). For stars on which both the longitudinal field and the field modulus have been measured, the field modulus is typically similar in magnitude to the longitudinal field. A comparable longitudinal field and field modulus hint at the presence of a large-scale ordered field in these slow rotators. A spatially intermittent field would have a much smaller ratio of the longitudinal field to the modulus, as is the case for the Sun, where variations in the line-of-sight field across the solar surface tend to cancel each other out.

Field strengths for the Ap stars, when variable, are observed to vary at the stellar rotation rate (Deutsch 1956; Preston 1971). The Ap stars appear to preferentially rotate more slowly than the normal A stars, with the possible exception of the early A stars (Abt 2000; Royer et al. 2007). Within the class of Ap stars, however, there is little or no correlation between magnetic field strength and rotation rate (e.g., Kochukhov & Bagnulo 2006). Such a lack of correlation is in contrast to what one might expect from fields generated by a core dynamo. Within the class of Ap stars, rotational periods range from decades to a fraction of a day, with typical periods on the order of a few days (e.g., Borra et al. 1982; Mestel 1999).

The variability and apparent large-scale organization of the magnetic fields observed in Ap stars have led to oblique rotator models (ORMs; Stibbs 1950; Mestel 1999). The ORM envisages a large-scale magnetic dipole, inclined to the rotation axis, frozen into the atmosphere of the star, and dragged along with the star as it rotates. This model is highly idealized, and modifications to a simple dipole are often required. The modulus measurements of Mathys et al. (1997) suggest a significant deviation from a purely dipolar geometry, with only one minimum and maximum present during a rotational cycle (as opposed to the two expected for a dipolar field). More recently, Kochukhov et al. (2004) showed that the spectrum of 53 Cam was well fit only after employing higher-order multipoles (spherical harmonic degree ℓ up to 15).

1.2. Possible Primordial Origin of Magnetism

The apparently static nature of the magnetic fields of Ap stars has led to the development of the fossil field theory. As originally pointed out by Cowling (1945) in the context of the Sun, a typical Ohmic decay time for a global-scale stellar magnetic field is longer than the lifetime of the star. The observed magnetic fields may then be a remnant of an interstellar field threading the cloud of gas from which the star formed. Recent observational surveys suggest that Ap stars exhibit markedly less magnetic flux as they near the end of their main-sequence lifetimes, possibly due to diffusive decay or reorganization of magnetic fields in the radiative zones of these stars (Kochukhov & Bagnulo 2006; Landstreet et al. 2008). The fossil theory may also help explain the slow rotation of Ap stars (relative to their non-magnetic counterparts) through magnetic braking of the star earlier in its lifetime (Mestel 1999). Such braking has been observed in magnetic Ae stars (the pre-main-sequence progenitors of Ap stars) which exhibit rotation rates about six times slower than the non-magnetic Ae stars (Alecian et al. 2008).

The structure of a typical fossil field has been a subject of speculation for some time. On the basis of stability arguments, these fields have generally been thought to be comprised of some form of linked poloidal and toroidal fields. Purely toroidal configurations have been shown by Tayler (1973) to be unstable to perturbations of azimuthal order $m = 1$, with the perturbations growing on the timescale needed for an Alfven wave to travel along the magnetic field line. A purely poloidal field has been shown to be unstable to nonaxisymmetric perturbations (e.g., Wright 1973; Markey & Tayler 1973; Flowers & Ruderman 1977). The analysis of Braithwaite (2007) suggests that rotation decreases the rate of growth of instability, but does not prevent the onset. Likewise Brun (2007) has studied the role of rotation on the onset of the poloidal instability and found that the most unstable wavenumber m increases with the rotation rate. A stable magnetic field configuration in the radiative zone must necessarily contain more twist than purely poloidal or toroidal configurations afford. Prendergast (1956) showed that such a linked, poloidal–toroidal configuration satisfied the criteria for equilibrium, but stopped short of proving the stability of such a field. More recently, Duez & Mathis (2009) have derived a linear stability analysis of the magnetic field configuration in a barotropic star, confirming the mixed toroidal–poloidal nature of the stable field.

The numerical simulations of Braithwaite & Spruit (2004) and Braithwaite & Nordlund (2006) for a nonrotating star have shown that a linked poloidal–toroidal field configuration is indeed stable on timescales commensurate with those of the star's evolution, and appears to be the preferred equilibrium condition for an initially random field. They found that a randomly oriented fossil field, present from the time of the star's appearance on the main sequence, will slowly relax into a twisted torus shape. The diffusion of this torus through the radiative zone into the nonconducting atmosphere of the star (which cannot support a twisted field) results in the appearance of a largely poloidal field at the stellar surface. They estimated this diffusion time to be around 2×10^9 yr, a time somewhat longer than the main-sequence lifetime of the star. The appearance and subsequent diffusion of this fossil field may also help to explain the observed middle-aged nature of the magnetic Ap stars (Kochukhov & Bagnulo 2006).

1.3. Dynamic Origins for Fields

The cores of A-type stars (roughly the inner 15% by radius), along with a thin shell at the surface, are known to be convective, and such core convection has long been suspected of achieving dynamo action (Krause & Oetken 1976). Brun et al. (2005, hereafter BBT05) have investigated this possibility through three-dimensional (3D) numerical simulations and found that the cores of A stars sustain vigorous dynamo action, with typical field strengths reaching near equipartition values with the convective kinetic energy. Core dynamos may have bearing on the surface fields observed in Ap stars through the production of magnetically buoyant structures. This possibility has been investigated through simulations by MacGregor & Cassinelli (2003) for more massive O and B stars, demonstrating that flux tubes may rise to the stellar surface in a time significantly less than the star's main-sequence lifetime. However, MacDonald & Mullan (2004) have pointed out that the inclusion of realistic compositional gradients into the model of MacGregor & Cassinelli would severely hinder the rise of flux tubes, ultimately requiring a very high field strength if a magnetic structure is to reach the stellar surface. Given that these fields are assumed to be produced by dynamo action in the core, their strengths would need to be well in excess of equipartition values, possessing magnetic energies at least 10 times greater than the convective kinetic energy.

Convection may also play a role in the early evolution of these stars' magnetic fields. The fully convective Hayashi phase that A stars are thought to undergo on their journey to the main sequence holds the potential for magnetic dynamo action. Fully convective dynamos have been found, for instance, by Dobler et al. (2006) and in 3D modeling of M-type stars (Browning & Basri 2007; Browning 2008). Surveys of Ae stars by Alecian et al. (2008) reveal the existence of observable magnetic fields in these stars following the Hayashi phase (but prior to the development of a convective core). Either these fields must have been present prior to a Hayashi phase and survived, or were generated by the convective motions present during that epoch. Dynamo activity during a Hayashi phase thus seems likely and may augment or alter any primordial magnetic fields.

Separately, the field instabilities noted in Section 1.2 could lead to dynamo action through interaction with prominent differential rotation, as suggested by Spruit (2002), though some complications with this mechanism have been raised by Zahn et al. (2007). The dynamo scenario envisioned by Spruit is unlikely to be operating in main-sequence Ap stars, since the surfaces of these stars are observed to be rotating as solid bodies. This mechanism may, however, have had a role in field generation at earlier epochs.

1.4. Interaction of Core Dynamo with the Fossil Field

While a primordial magnetic field seems to be the likely source for the surface magnetism observed on Ap stars, convection may also be implicated. Whether during the Hayashi phase early in the star's lifetime, or during the main-sequence phases, convection and associated dynamo action may have a role in the magnetic fields that are observed. This leads to several basic questions. What is the nature of the interaction between a primordial field and one generated contemporaneously by a core dynamo? Does a strong fossil magnetic field help or hinder dynamo action, and does the dynamo have any significant effect on the configuration of the fossil field? Kinematic modeling by Moss (2004) suggests that a sufficiently strong exterior field could hinder the dynamo action in the core. Although instructive, this axisymmetric model does not capture the complex 3D processes likely to be occurring within the core.

We are thus motivated to turn to detailed modeling of the coupling of a fossil field and convective core dynamo within an A-type star. The nonlinear 3D simulations used here allow us to assess both the growth and equilibration of the magnetic fields, and also the feedback of such fields on the nature of flows within the core. Our results provide some insights into the interaction between an exterior fossil field and the stellar core dynamo, demonstrating that the presence of a fossil field holds out possibilities for enhanced dynamo action.

We shall discuss elements of our 3D modeling approach in Section 2. Then in Section 3, we review the behavior of core dynamo action realized in BBT05, and in Section 4 how the overall magnetic and kinetic energy balance is modified in the new dynamo state eventually achieved after having introduced a mixed poloidal/toroidal external field. Starting in Section 5 we begin to analyze various elements of the flows and magnetic field structures that characterize the super-equipartition state that we have realized in which the magnetic energy can be 10-fold greater than the convective kinetic energy. In Section 10, we examine the processes responsible for the generation and maintenance of these strong magnetic fields. In Section 11, we examine effects of multipolar fossil fields, and then in Section 12 we reflect on the significance of finding such super-equipartition dynamo behavior.

2. SIMULATION ELEMENTS

2.1. Anelastic MHD Approach

Our numerical simulations are carried out using the anelastic spherical harmonic (ASH) code which is described in detail in Clune et al. (1999) and in Brun et al. (2004). ASH is a pseudo-spectral code designed to perform efficiently on massively parallel supercomputers and solves the 3D magnetohydrodynamic (MHD) equations in a rotating spherical shell. The anelastic approximation assumes that fluid motions are subsonic and that perturbations to thermodynamic variables are small compared to their mean, horizontally averaged values at a given depth in the fluid (Gough 1969; Gilman & Glatzmaier 1980). Within the anelastic approximation, the thermodynamic variables are linearized about their spherically symmetric and evolving mean state with density $\bar{\rho}$, pressure $\bar{P}$, temperature $\bar{T}$, and specific entropy $\bar{S}$. Fluctuations about this state are denoted as ρ, P, T, and S. In the uniformly rotating reference frame of the star, the MHD equations are expressed as

$$\nabla \cdot (\bar{\rho}\boldsymbol{v}) = 0, \tag{1}$$

$$\nabla \cdot \boldsymbol{B} = 0, \tag{2}$$

$$\bar{\rho}\left[\frac{\partial \boldsymbol{v}}{\partial t} + (\boldsymbol{v}\cdot\nabla)\boldsymbol{v} + 2\boldsymbol{\Omega}_0 \times \boldsymbol{v}\right] = -\nabla P + \rho \boldsymbol{g} + \frac{1}{4\pi}(\nabla \times \boldsymbol{B}) \times \boldsymbol{B} - \nabla \cdot \mathcal{D} - [\nabla \bar{P} - \bar{\rho}\boldsymbol{g}], \tag{3}$$

$$\bar{\rho}\bar{T}\frac{\partial S}{\partial t} + \bar{\rho}\bar{T}\boldsymbol{v}\cdot\nabla(\bar{S}+S) = \nabla\cdot[\kappa_r \bar{\rho} c_p \nabla(\bar{T}+T) + \kappa\bar{\rho}\bar{T}\nabla(\bar{S}+S)] + \frac{4\pi\eta}{c^2}\boldsymbol{j}^2 + 2\bar{\rho}\nu\left[e_{ij}e_{ij} - \frac{1}{3}(\nabla\cdot\boldsymbol{v})^2\right] + \bar{\rho}\epsilon, \tag{4}$$

$$\frac{\partial \boldsymbol{B}}{\partial t} = \nabla \times (\boldsymbol{v}\times\boldsymbol{B}) - \nabla\times(\eta\nabla\times\boldsymbol{B}). \tag{5}$$

The velocity $\boldsymbol{v}$ expressed in spherical coordinates is $\boldsymbol{v} = (v_r, v_\theta, v_\phi)$ relative to a frame rotating at constant angular velocity $\boldsymbol{\Omega}_0$, $\boldsymbol{g}$ is the gravitational acceleration, $\boldsymbol{B} = (B_r, B_\theta, B_\phi)$ is the magnetic field, $\boldsymbol{j} = c/4\pi(\nabla\times\boldsymbol{B})$ is the current density, c_p is the specific heat at constant pressure, κ_r is the radiative diffusivity, η is the effective magnetic diffusivity, and $\mathcal{D}$ is the viscous stress tensor given by

$$\mathcal{D}_{ij} = -2\bar{\rho}\nu\left[e_{ij} - \tfrac{1}{3}(\nabla\cdot\boldsymbol{v})\delta_{ij}\right], \tag{6}$$

where e_{ij} is the strain rate tensor, and ν and κ are effective eddy diffusivities. We have chosen to represent the energy generation by nuclear burning of the CNO cycle with a volumetric heating term $\overline{\rho}\epsilon$ (see Section 2.3 for details). This set of equations is closed by assuming the thermodynamic fluctuations satisfy the linear relations

$$\frac{\rho}{\bar{\rho}} = \frac{P}{\bar{P}} - \frac{T}{\bar{T}} = \frac{P}{\gamma\bar{P}} - \frac{S}{c_p}, \tag{7}$$

assuming the ideal gas law

$$\bar{P} = \mathcal{R}\bar{\rho}\bar{T}, \tag{8}$$

where $\mathcal{R}$ is the gas constant. In this MHD context, the anelastic approximation also filters out the fast magneto-acoustic modes. Alfven modes, as well as the slow magnetosonic modes are retained. The divergence-free nature of the mass flux and of the magnetic field is maintained through the use of a toroidal–poloidal decomposition whereby

$$\bar{\rho}\boldsymbol{v} = \nabla\times\nabla\times(W\boldsymbol{e}_r) + \nabla\times(Z\boldsymbol{e}_r), \tag{9}$$

$$\boldsymbol{B} = \nabla\times\nabla\times(C\boldsymbol{e}_r) + \nabla\times(A\boldsymbol{e}_r). \tag{10}$$

The stream functions W and Z, as well as the magnetic potentials C and A, are functions of all three spatial coordinates and time; $\boldsymbol{e}$ is the unit vector.

This set of equations in the six variables W, Z, C, A, S, and P requires 12 boundary conditions to be well posed. We have chosen to impose the following boundary conditions throughout the simulation:

1. Impenetrable top and bottom surfaces in the deep shell: $v_r = 0$.
2. Stress-free top and bottom: $(\partial/\partial r)(v_\theta/r) = (\partial/\partial r)(v_\phi/r) = 0$.
3. Constant entropy gradient at top and bottom: $\partial \bar{S}/\partial r =$ constant.
4. Perfect conductor top and bottom: $B_r = (\partial/\partial r)(B_\theta/r) = (\partial/\partial r)(B_\phi/r) = 0$.

These conditions ensure that no mass or angular momentum is lost from the system via either radial momentum flux or torques arising from viscous or magnetic stresses at the upper and lower boundaries of the deep spherical shell being studied. Emergent flux through the top and the bottom remains constant in time, but differs between the two boundaries to account for energy generation in the core. The leakage of magnetic energy from the domain is prevented by forcing the Poynting flux to vanish at the boundaries. Other boundary conditions, especially for the magnetic fields, could be imposed, but at this stage these appear to be the most neutral, particularly at the lower boundary where strong magnetic fields are generated.

2.2. Implementation of ASH

Seeking to deal with full spherical global domains, ASH is a large-eddy simulation (LES) code, with subgrid-scale (SGS) descriptions for dynamics occurring on scales below the spatial resolution of the simulations. We have chosen to focus on the larger scales of flow, believing that they are most likely to be responsible for establishing the mean properties of core convection and dynamo action. In the solar context, this approach has been reasonably successful in making contact with helioseismic deductions of the solar interior differential rotation (Brun & Toomre 2003; Miesch et al. 2006, 2008), and has been shown in the A star context (BBT05) to produce sustained dynamo action. Here we treat the SGS terms most simply as enhancements to the kinematic viscosity as well as to the thermal and magnetic diffusivities. Much as in BBT05, we have defined our eddy viscosity and diffusivities to be a function of the mean density alone (and hence radius), independent of horizontal position or time. Specifically, we have taken these quantities to be proportional to $\overline{\rho}^{-1/2}$.

ASH's numerical implementation involves expanding all variables in spherical harmonics $Y_l^m(\theta, \phi)$ in the horizontal directions and Chebyshev polynomials in the radial direction. To gain higher resolution at the interface between the convective and radiative zones, and thus to better resolve the penetrative convection occurring in this region, we have employed a stacked Chebyshev scheme. In doing so, we have split the computational domain into two separate regions (radially) and performed separate Chebyshev expansions for each region. The spherical harmonic expansion is truncated at degree $\ell_{\max}$, with all azimuthal orders m retained in a triangular truncation, ensuring that we have uniform resolution over spherical surfaces. For our simulations, we have taken $\ell_{\max} = 170$, corresponding to 256 mesh points in the latitudinal direction (N_θ), with the longitudinal mesh having $N_\phi = 2N_\theta$, and in radius $N_r = 49 + 33 = 82$. The time evolution of our simulations is computed using an implicit, second-order Crank–Nicolson scheme for the linear terms and an explicit second-order Adams–Bashforth scheme for the advective, Coriolis, and Lorentz terms. The computational demands of these calculations are substantial, and thus the ASH code has been optimized to run on massively parallel supercomputers, using the message passing interface (MPI) to communicate between different computational nodes.

2.3. Modeling the A-type Star

We have chosen to model the inner 30% by radius of a main-sequence A-type star of 2 $M_\odot$ rotating at four times the mean solar rate of $\Omega_0 = 414$ nHz. The mean rotation period is thus about 7 days. The emerging luminosity of this star is 19 $L_\odot$. The inner 2% of the star by radius has been excluded to avoid the coordinate singularity at $r = 0$. This model consists of a convective core occupying the inner 15% by radius of the star with an overlying radiative zone extending to the outer radius of our computational domain. The density contrast across the full domain is 21.5, and that across the convective core is 2.04.

All models presented here were initialized using the statistically mature case C4m of BBT05. The convection and associated dynamo action involved complex flows and magnetism that were continuously evolving and rebuilding structures, but the overall system had equilibrated in terms of its time-averaged properties such as energies and differential rotation. Case C4m was evolved from a one-dimensional stellar structure model (at an age of 500 Myr) computed with the CESAM stellar evolution code (Morel 1997) using realistic microphysics and employing a classical mixing-length formalism to describe the convection. A necessary modification to this model was the softening of the entropy gradient in going from the convective core to the radiative zone. The stark contrast in entropy between these two regions would otherwise result in the driving of high-frequency internal gravity waves which would severely limit the time steps. The principal input parameters are the same for the simulations presented here as for their progenitor case. As in BBT05, the energy generation term ϵ was implemented as $\epsilon = \epsilon_0 \overline{T_6}^8$, with $\epsilon_0 = 6.0 \times 10^{-9}$ erg g^{-1} s^{-1}. Furthermore, we have taken the thermal diffusivity κ to be 4.0×10^{12} cm^2 s^{-1} at the top of the domain. Similarly, there the SGS viscosity is $\nu = 1.0 \times 10^{12}$ cm^2 s^{-1} and the magnetic diffusivity is $\eta = 2.0 \times 10^{11}$ cm^2 s^{-1}. Thus our effective Prandtl number Pr = 0.25, and our magnetic Prandtl number is Pm = 5.0. These values were chosen to achieve a high magnetic Reynolds number Rm at reasonable computational cost and to facilitate comparison with BBT05. Using rms velocities and magnetic field strengths at mid-core and a length based on the core depth, the Reynolds number Re for our primary case A following equilibration is 136, and the corresponding magnetic Reynolds number Rm is 680. The associated Rossby number for this case is Ro $= 6 \times 10^{-3}$.

2.4. Imposing a Fossil Magnetic Field

All simulations here have been initialized by superimposing external magnetic fields of varying geometries onto the existing field structure of case C4m of BBT05 at a time corresponding to day 2000 of that simulation. Our choices for the initial magnetic configuration in each case have been motivated by stability considerations and the need to sort out the role that the toroidal and poloidal components of the imposed magnetic field have in the overall response.

We have chosen a mixed poloidal–toroidal magnetic field (case A), a poloidal field (case B), and a purely toroidal magnetic field (case C) for our initial external field configurations. To disentangle the effects of spatial scale of the field, we have also examined external field configurations with higher-order multipolar structure (lacking a toroidal component) in which each hemisphere receives zero net magnetic flux across the interface between the convective core and the radiative zone.

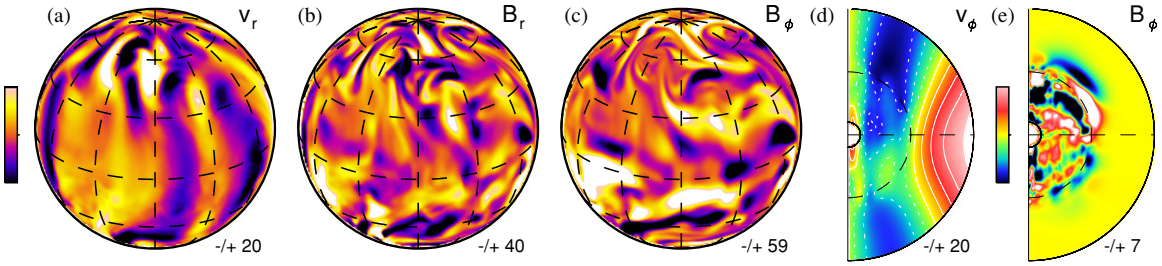

Figure 1. Flow and magnetic field properties of the core convection dynamo in the progenitor case C4m. (a) Snapshot of radial velocity at mid-core ($r = 0.10R$), showing some columnar alignment of wavering rolls with rotation axis (upright). Regions of upflow are shown in light tones, downflows in dark tones; ranges in m s^{-1}. (b) Companion snapshot of radial magnetic field at mid-core, with a stronger field roughly coincident with downflows. Positive fields denoted by light tones, negative by dark; ranges in kG. (c) The azimuthal magnetic field B_ϕ at mid-core with some extended ribbon-like structures running east–west. (d) Mean zonal velocity $\langle v_\phi \rangle$ in radius and latitude possessing a central column of slower rotation. Prograde flow shown in red tones, retrograde in blue tones; ranges in m s^{-1}. (e) Mean azimuthal magnetic field $\langle B_\phi \rangle$ with a complex structure evident and exhibiting no preferred sense in either hemisphere. Positive field in red tones, negative in green/blue; ranges in kG.

(A color version of this figure is available in the online journal.)

The toroidal field for cases A and C was defined as

$$B_\phi = A \exp\left(-\frac{(\boldsymbol{r} - \boldsymbol{r_0})^2}{2\sigma^2}\right), \tag{11}$$

where r_0 lies along the equator at $0.225R$, σ is taken to be $2r_0$, and the amplitude A is taken to be 30 kG.

Our mixed-field case A included the same functional form for B_ϕ but with an added poloidal field consistent with a current threading through the center of the magnetic torus. The strength of the poloidal field was adjusted so that the ratio of energy in the poloidal field to that in the toroidal field was 1:9, as suggested by the results of Braithwaite & Nordlund (2006). Placing such a mixed field into C4m resulted in only a 10% increase to the total magnetic energy of that system. The purely toroidal and purely poloidal cases were also studied for comparison. In those cases, the field geometry and strength were identical to that component in the mixed-field case. Due to stability considerations, it is the mixed-field case A that appears to be the most physically relevant. As such, we have focused the bulk of our computational efforts and analyses on that case.

3. CORE DYNAMO IN PROGENITOR

Some key aspects of the progenitor dynamo simulation case C4m are summarized in Figure 1 illustrating the typical flows and fields achieved at one instant of time. These flows have been sampled at mid-core ($r = 0.1R$) and are displayed on spherical shells. In addition, we have sampled the differential rotational profile and mean fields realized in this system (Figures 1(d) and (e)), where the azimuthal velocity v_ϕ and the magnetic field B_ϕ have been averaged over longitude and displayed as a function of radius and latitude.

Case C4m of BBT05 involved highly time-dependent flows with complex, vigorous convection that penetrated substantially into the overlying radiative zone. These flows are characterized by convective motions spanning multiple scale heights that serve to couple widely separated parts of the computational domain. These convective motions give rise to a nearly adiabatically stratified core slightly prolate in shape. The prolate shape owes to the greater effect of the Coriolis force on radial velocities at the lower latitudes (see the discussion in BBT04). Surrounding the convective core is a further region of overshooting, roughly spherical in shape, which does not substantially modify the stable stratification of the radiative zone. A striking change in case C4m compared to its own hydrodynamic progenitor is the significant suppression of the differential rotation in the core. The hydrodynamic case has a prominent column of slow rotation maintained primarily by Reynolds stresses arising from the convection that transport angular momentum equatorward and radially outward. These counteract viscous stresses that transport angular momentum poleward and radially inward.

The addition of a seed dipole magnetic field to that hydrodynamic case to yield case C4m, as discussed in BBT05, resulted in a marked change to the differential rotation of the system. The dynamo action achieved by this system produces Maxwell stresses that tend to transport angular momentum poleward, opposing the Reynolds stresses and ultimately disrupting the differential rotation. There remains a weak column of slower (retrograde) rotation (Figure 1). The persistent dynamo action realized in this simulation yields nearly equipartition magnetic energies, with those about 90% of the kinetic energy. The magnetic energy in this system is largely comprised of fluctuating (nonaxisymmetric) fields, with the axisymmetric poloidal and toroidal fields contributing little to the overall energy balance. Both the magnetic fields and flows in case C4m are highly intermittent in time, with no evident preferred field polarity.

4. MODIFIED DYNAMO ACTION

A preliminary assessment of the dynamo action achieved in our 3D simulations is provided by examining the evolving global energy balances achieved in each case. The kinetic energy density (KE) is defined as

$$\mathrm{KE} = \tfrac{1}{2}(\overline{\rho} + \rho)\left(v_r^2 + v_\theta^2 + v_\phi^2\right), \tag{12}$$

and the magnetic energy density (ME) as

$$\mathrm{ME} = \frac{1}{8\pi}\left(B_r^2 + B_\theta^2 + B_\phi^2\right). \tag{13}$$

The azimuthal velocity v_ϕ is taken relative to the rotating frame. We find it useful to examine a number of decompositions of ME. To facilitate contact between our work and previous dynamo modeling, we are often interested in mean fields and flows and the fluctuations about those means. We thus adopt the following notation for the fluctuating (nonaxisymmetric) velocities:

$$\boldsymbol{v'} = ((v_r - \langle v_r \rangle)\boldsymbol{e}_r + (v_\theta - \langle v_\theta \rangle)\boldsymbol{e}_\theta + (v_\phi - \langle v_\phi \rangle)\boldsymbol{e}_\phi. \tag{14}$$

Angular brackets denote averages in azimuth (longitude). The fluctuating magnetic field vector $\boldsymbol{B'}$ is defined likewise. The

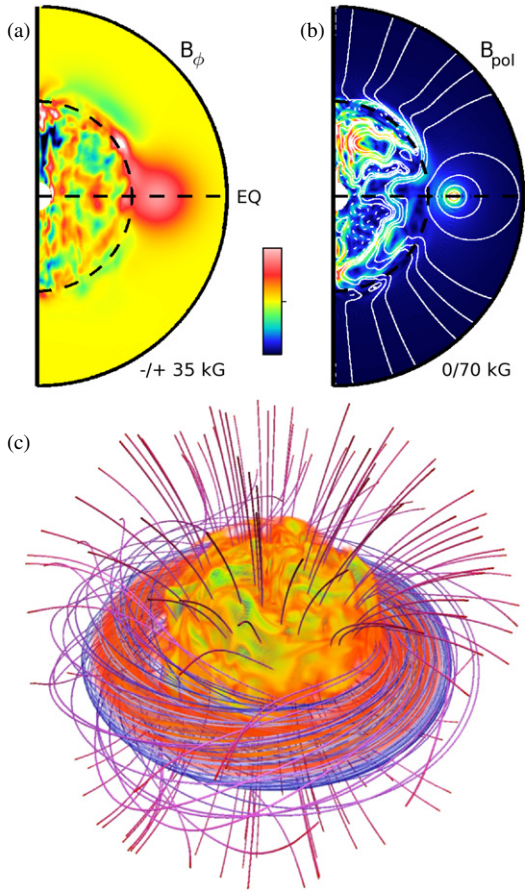

Figure 2. Superposing a fossil field into the progenitor case to initiate case A. (a) Azimuthally averaged B_ϕ at the initial instant and (b) the companion poloidal field. White lines denote poloidal field lines, and the underlay the poloidal field modulus. (c) Magnetic energy density shown volume rendered, with the imposed field forming the outer torus of moderate field strength. Field lines correspond to those of the fossil field only.

(A color version of this figure is available in the online journal.)

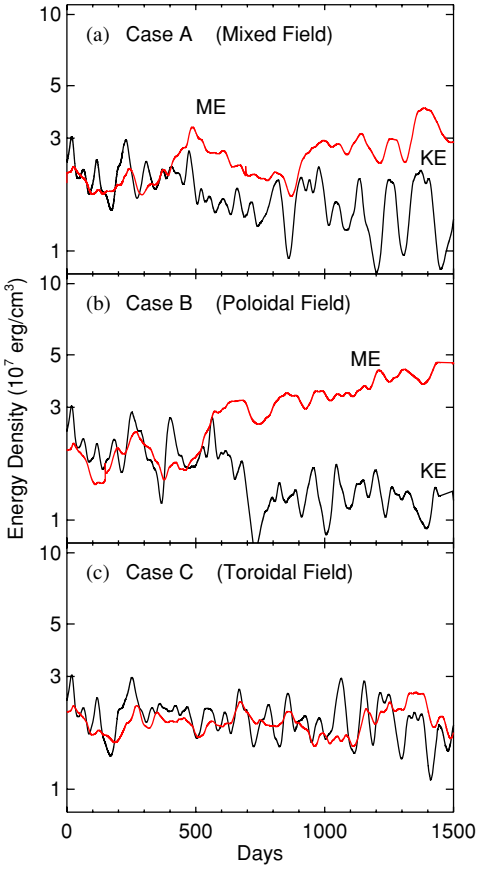

Figure 3. Separating the role of flux and helicity. (a) Temporal evolution of the mixed-field case A. Volume-averaged ME is shown in red and KE in black. (b) Temporal evolution for the poloidal field case B. (c) Evolution of the purely toroidal field case C. Cases A and B exhibit a tendency for transition to super-equipartition. Case C exhibits no such behavior, suggesting that the inclusion of a poloidal magnetic field spurs the transition.

(A color version of this figure is available in the online journal.)

magnetic energy is further decomposed into those portions associated with the mean toroidal fields (MTE), the mean poloidal fields (MPE) and the fluctuating nonaxisymmetric fields (FME). We define these quantities as

$$\mathrm{MTE} = \frac{1}{8\pi}\langle B_\phi\rangle^2, \tag{15}$$

$$\mathrm{MPE} = \frac{1}{8\pi}(\langle B_r\rangle^2 + \langle B_\theta\rangle^2), \tag{16}$$

and

$$\mathrm{FME} = \frac{1}{8\pi}[(B_r')^2 + (B_\theta')^2 + (B_\phi')^2]. \tag{17}$$

We also find it useful to distinguish between the magnetic energy in the fluctuating ϕ component of the field (FTE) and that in the fluctuating r and θ components (FPE), with

$$\mathrm{FTE} = \frac{1}{8\pi}(B_\phi')^2 \tag{18}$$

and

$$\mathrm{FPE} = \frac{1}{8\pi}[(B_r')^2 + (B_\theta')^2]. \tag{19}$$

The superposition of our twisted fossil magnetic field into case C4m, involving the introduction of both toroidal and poloidal components, and denoted here as the mixed-field case A, is shown in Figure 2 at the outset. A magnetic field has been added primarily into the radiative zone, but there is some threading of the field near the equator into the convective core. There ensues a notable departure of behavior in our mixed-field system from that of the progenitor case C4m. This is readily apparent in the systematic evolution of kinetic and magnetic energies (Figures 3(a) and 4). The KE, ME, and MTE shown here have been averaged over the full computational domain. We have also studied the early response of the system to either the introduction of the external purely poloidal field (case B, Figure 3(b)) or of a purely toroidal field (case C, Figure 3(c)). Variations in ME and KE occur on the dynamical timescale (i.e., the overturning time of roughly 100 days) in each case. It is evident that the toroidal field has little effect, whereas the purely poloidal field leads to a more rapid early growth in ME than the mixed-field case A. This suggests that the presence of a poloidal component, and not the twist (helicity) of the external field, is an important ingredient leading to significant growth in overall ME. However, since it has been argued that neither a purely toroidal nor a purely poloidal field would survive in the radiative exterior, we shall hereafter concentrate on the stable mixed-field case A.

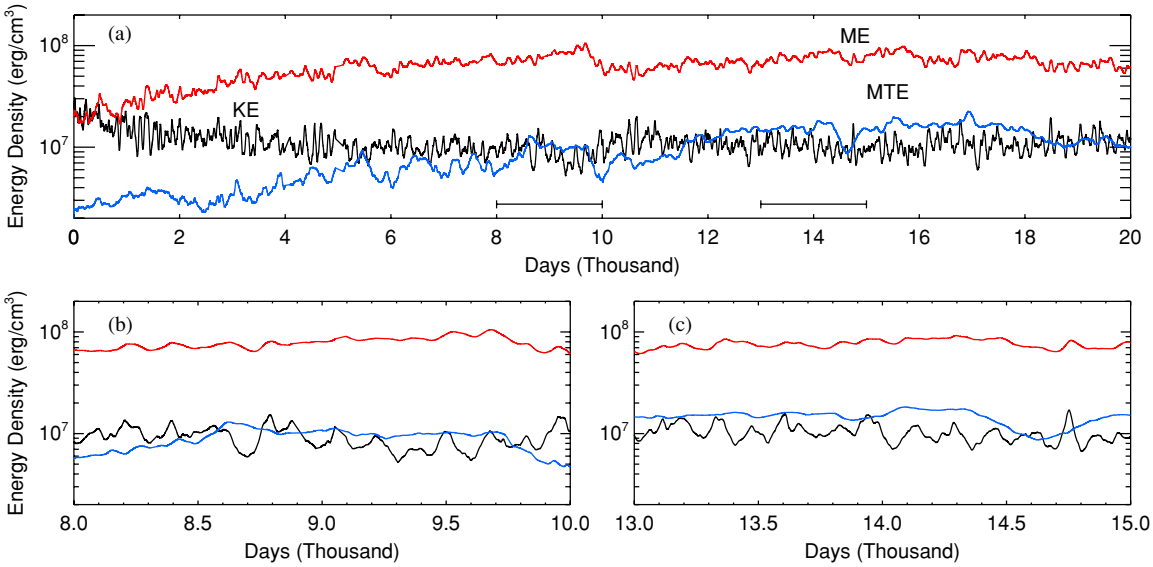

Figure 4. Temporal evolution of overall energy densities (volume averaged) in case A after imposition of an external mixed magnetic field. (a) Full evolution sequence over 20,000 days (or about 2900 rotation periods), revealing that the ME (red) has grown in strength to become about 10-fold greater than the KE (black). The mean toroidal field magnetic energy MTE ME (blue) has also increased prominently in strength, attaining in (b) roughly equipartition levels with KE in the close-in view starting at 8000 days, and (c) slightly super-equipartition behavior in the interval starting at 13,000 days.

(A color version of this figure is available in the online journal.)

4.1. Temporal Evolution of Energies in Case A

The full evolution of case A is shown in Figure 4. Following the imposition of our fossil magnetic field (constituting only about a 10% increase in ME), the overall ME (volume integrated) of case A undergoes a phase of gradual growth. This growth of ME continues for approximately one magnetic diffusion time across the core radius (∼7000 days), at which point the system reaches a saturation level of ME/KE ∼10. Over the roughly three diffusion times (and many hundreds of dynamical times) we have evolved this case, the ratio ME/KE is highly intermittent in time, varying on timescales of a few hundred days. It reaches a peak of about 16 near day 10,000, followed by a rapid decline to more typical values. Such behavior is in marked contrast to that of the progenitor case C4m where approximate equipartition of magnetic and kinetic energies was maintained throughout the simulation.

The energy balance here is achieved through a roughly fourfold rise in ME, along with a twofold decrease in KE. The growth of ME is accompanied by a similar growth of axisymmetric (mean) toroidal fields (MTE) which generally account for about 10%–20% of the total ME, much as in the progenitor solution. A steady rise in MTE continues until approximate equipartition with respect to KE is reached. By contrast, the energy in the axisymmetric poloidal fields (not shown) comprises about 5% of the total ME on average. Axisymmetric toroidal fields undergo a brief phase of super-equipartition of their own near 15,000 days. Such equipartition and super-equipartition behavior of the mean fields are examined in expanded temporal detail in Figures 4(b) and (c), respectively. Here KE and ME both vary on timescales of 100–200 days. By contrast, MTE varies on timescales of 500–1000 days and follows the long-term trends in ME. Shorter trends in ME are due largely to nonaxisymmetric (fluctuating) magnetic fields within the core which vary on timescales commensurate with the convection. The axisymmetric fields are stored largely within the lower radiative zone where flows are much more quiescent. Diffusive processes play a more dominant role in the evolution of the magnetic field there, resulting in slower evolutionary trends for MTE. The variation in KE in the two extracted closeups of the time series (Figures 4(b) and (c)) is modest despite the different MTE, in large part because the bulk of kinetic energy for this system is convective and concentrated within the core. Convective motions and axisymmetric fields thus interact largely near the convective core and radiative zone interface, which includes the region of overshooting.

5. DYNAMICS OF THE SUPER-EQUIPARTITION STATE

The spatial structuring in the velocity and magnetic fields within the super-equipartition states realized by dynamo action in case A is relatively complex in order to avoid strong Lorentz forces that would otherwise seek to quench the flows. We now examine the nature of such structures and their implications for the overall dynamics.

5.1. Overall Properties

Strong magnetic fields generated in our mixed-field case A are present fairly uniformly throughout the convective core. The convection continues to exhibit broad upflows and downflows spanning much of the convection zone, with smaller scale motions present in the region of overshooting. A snapshot of the evolving flows and magnetic fields is shown in Figure 5, sampling radial velocities and both radial and azimuthal magnetic field components both at mid-core ($r = 0.10R$) and in the overshooting region ($r = 0.16R$) at around day 15,000. Velocities and magnetic fields at mid-core are shown in both orthographic view (with the north pole tilted into view), and also rendered in Mollweide projection, with the full spherical surface thus visible. In the latter rendition, lines of latitude are denoted by horizontal lines (equator at middle), and those of longitude by curved lines. The radial velocity patterns (Figures 5(a) and (d)) indicate roll-like motions roughly aligned with the rotation axis and involving about 4–6 rolls. These rolls extend from pole to pole, maintaining their coherence across both hemispheres.

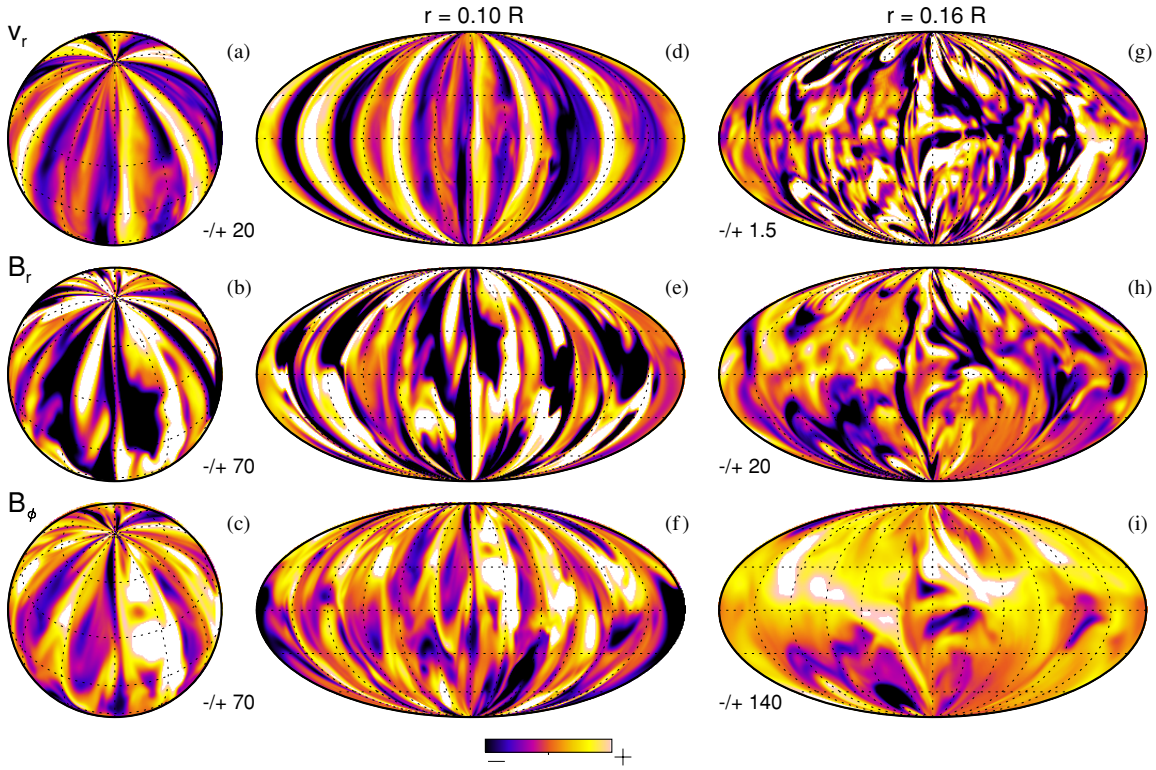

Figure 5. Snapshot of radial velocity v_r (upper panels) and the two magnetic field components B_r and B_ϕ (middle and lower panels) for the mixed-field case A at about day 15,000. The tilted orthographic views (left column) and Mollweide projection are sampled at mid-core ($r = 0.10R$; left and center columns), and in the region of overshooting near the core and radiative zone interface ($r = 0.16R$; right column). Using a common color table, velocity ranges are indicated in m s^{-1} and magnetic field sense and strength in kG; yellow tones are positive, dark violet are negative.

(A color version of this figure is available in the online journal.)

Such behavior contrasts with that of the progenitor where convective rolls tend to waver in latitude (Figure 1(a)). Flows in case A exhibit somewhat smaller amplitudes than those of the progenitor case. Typical convective velocities (based on rms velocity at mid-core) for case A are ∼20 m s^{-1} versus ∼29 m s^{-1} before the external field was imposed. The radial velocity pattern in the region of overshooting (Figure 5(g)), compared to mid-core, involves smaller scales and less alignment, consistent with intermittent upward penetration by plumes, which involve roughly 10-fold weaker velocities.

The accompanying radial magnetic fields for case A at mid-core (Figures 5(b) and (e)) and in the region of overshooting (Figure 5(h)) exhibit similar patterns to that seen in the convective flows. These magnetic structures are less spatially intermittent than their counterparts in BBT05. Azimuthal magnetic fields display similar behavior (Figures 5(c), (f), and (i)) and exhibit much less banding within the core than that observed in the progenitor case. Typical magnetic field strengths at mid-core are roughly 80 kG, or about 20% higher than those present prior to imposing the fossil field. Regions of prominent azimuthal and radial fields exhibit approximate antisymmetry about the equator. The simplified magnetic geometry within the core in case A is suggestive of a columnar, helical magnetic field topology unlike that seen in the progenitor case C4m.

Near the edge of the convective core, some rotational shearing still exists in the transition from weak differential rotation in the core to nearly solid body rotation in the radiative exterior. The strong B_ϕ (Figure 5(i)) fields trace out the boundaries of the largest convective rolls. Shearing and stretching in the overshooting region allow these structures to grow into ribbons of a field that wrap their way poleward around the cylindrical convective rolls. Magnetic field strengths within the centers of these ribbons are about 200 kG.

5.2. Complex Interplay of Flows and Field Structures

The intricate configurations of the strong magnetic fields realized in case A are clarified by Figure 6 showing 3D volume renderings of the magnetic energy and tracings of the magnetic field lines, sampling the same time instant as in Figure 5. Magnetic energy throughout the convective core and the region of overshooting is presented in Figure 6(a). The regions of strong ME (denoted by green/orange tones) reach from the equator to pole in long helical arcs. Toroidal structures are visible here as well, with magnetic energy tending to wrap around convective columns parallel to the rotational axis rather than the entire core. These impressions are accentuated in magnetic field line tracings (Figure 6(b)), showing complex wrappings around the convective cells. Other volume renditions involve a narrow slice in the equatorial plane, sampling again the ME (Figure 6(c)) and the KE (Figure 6(d)). Here we view the equatorial plane as if from the north pole. The strong flux ropes (about 200 kG in strength) extend throughout much of the core, tracing out the pattern of the most prominent convective rolls found there. Regions of blue indicate strong (∼ 300 kG) regions of the magnetic field. These strong fields are part of extended helical arcs (Figure 6(b)). The accompanying kinetic energy rendition (Figure 6(d)) reveals that the strongest fields are laterally displaced from the fastest flows, recognizing that otherwise Lorentz forces may tend to suppress the flows unless the velocity and magnetic fields exhibit some measure of alignment (see Section 10).

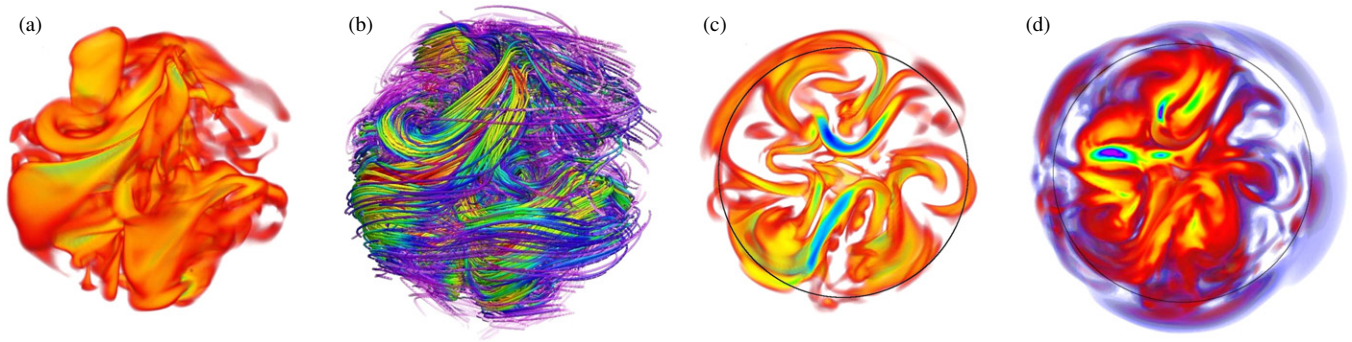

Figure 6. Volume rendering of magnetic structures (with rotation axis vertical) near day 15,000 accompanying Figure 5. (a) Magnetic energy density realized in the convection zone and region of overshooting; yellow/green tones indicate high values, and red tones indicate low values. (b) Magnetic field lines traced throughout the convection zone. Yellow/red tones correspond to high field strengths, violet/blue tones to low. Strong flux ropes coincide with regions of high magnetic energy. (c) ME rendered in the equatorial plane viewed as if from the north pole, with greatest energy levels shown in blue/green. (d) Companion KE rendered in the equatorial plane showing that the fastest flows are positioned adjacent to the sides of the regions of strongest field, with blue/green again highest energy density.

(A color version of this figure is available in the online journal.)

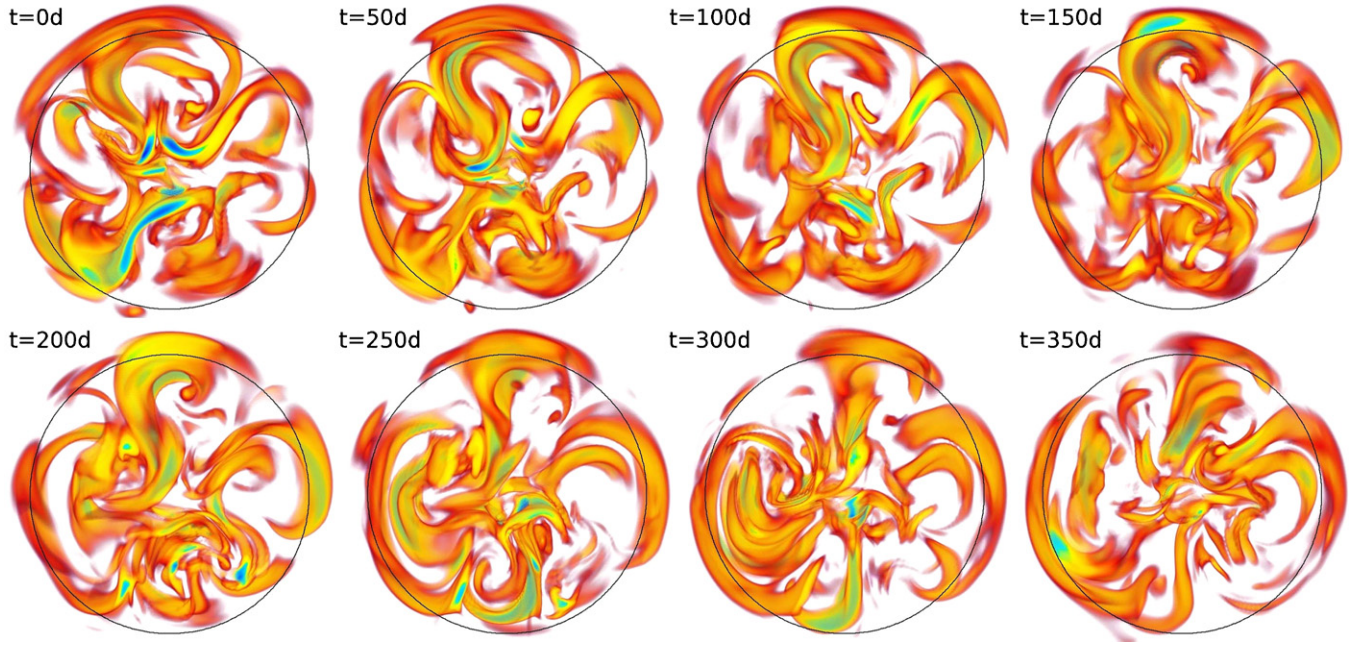

Figure 7. Sequence of views showing the evolution of ME in narrow volume renderings of the equatorial plane, starting from day 15,000 (as in Figure 6(c)). Green/yellow tones denote high values, red tones denote low values. Magnetic features stretch, strengthen, and at times join with those created by adjoining convective rolls.

(A color version of this figure is available in the online journal.)

These dynamic structures in magnetic energy evolve on timescales of about 100 days. A sense of these intricate changes is provided by Figure 7 by sampling the evolution of magnetic fields in the equatorial plane over a 350-day interval. Here close inspection reveals that magnetic structures are seen to rise radially, stretch, and ultimately dissipate. At times large bundles of magnetic flux cleave into each other, forming tubular structures that encircle much of the convection zone at the equator.

5.3. Statistical Properties of The Super-equipartition State

Topological differences in magnetic fields and flows between case C4m and case A may be further characterized through probability distribution functions (pdf's) of $\boldsymbol{v}$ and $\boldsymbol{B}$, as shown in Figure 8 for the velocity and magnetic field at mid-core. Magnetic fields (Figures 8(b) and (d)) peak at higher values and exhibit a noticeably greater range of variability in case A than in case C4m. This broadening, related to the spatial intermittency, may be quantified by measuring the kurtosis $\mathcal{K}$ (the fourth moment) of these curves. A large value of $\mathcal{K}$ indicates a broad distribution, and a low value indicates a narrow one. We find that $\mathcal{K}$ for B_r has transitioned from a value of 4.4 in case C4m to 6.7 in case A. The convective core of case A is thus pervaded more uniformly by a strong magnetic field than in case C4m. The converse is true for the velocity distributions (Figures 8(a) and (c)), which are narrower and peak at lower values in case A relative to case C4m. Correspondingly, the $\mathcal{K}$ for v_r has transitioned from 4.4 in C4m to 4.1 in case A. The most vigorous downflows in case A are somewhat weaker than those in case C4m which exhibits a more prominent negative tail in v_r.

6. GROWTH OF AXISYMMETRIC HELICAL FIELDS

The super-equipartition state achieved in case A involves the generation of strong axisymmetric (mean) magnetic structures well beyond that achieved in the absence of an external fossil field. Figure 9 shows the profiles with radius and latitude of the

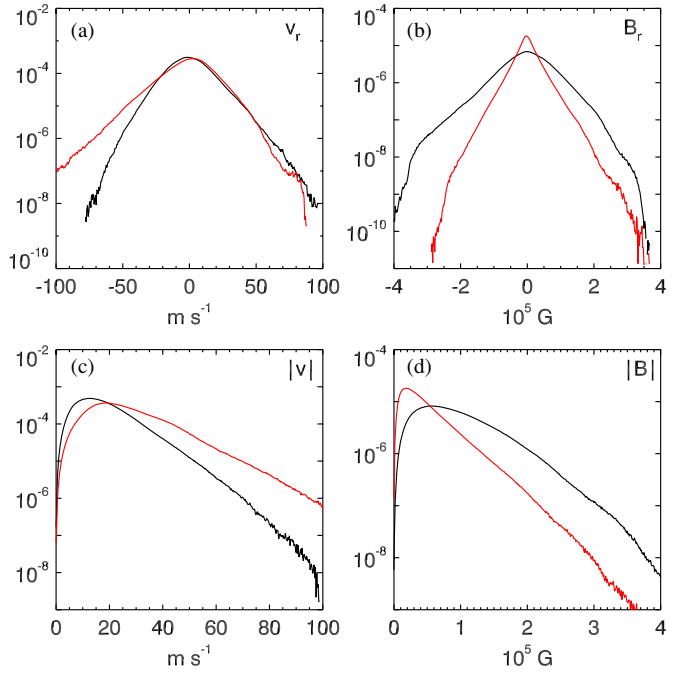

Figure 8. Time-averaged pdf's for case A (black) and case C4m (red) of velocities (V_r and $|V|$) and magnetic fields (B_r and $|B|$) sampled on a spherical surface at mid-core ($r = 0.10R$). Case A is characterized by narrower velocity distributions and broader magnetic field distributions than case C4m.

(A color version of this figure is available in the online journal.)

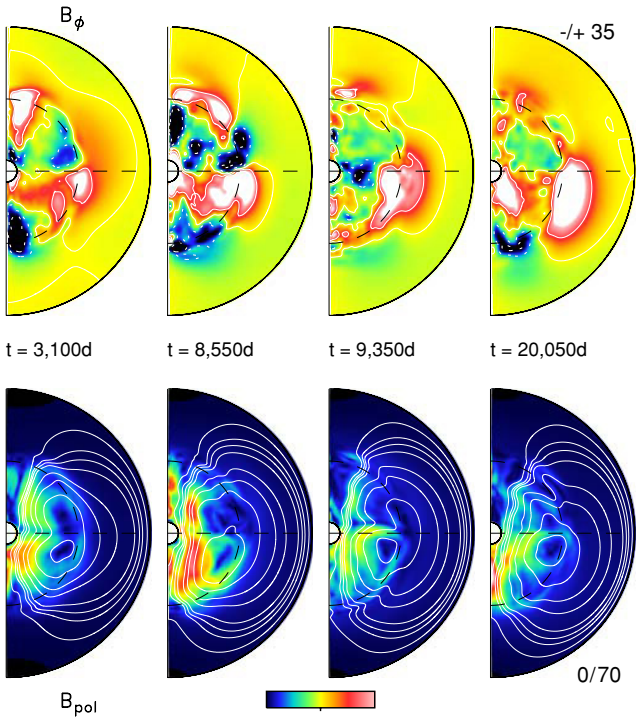

Figure 9. Temporal evolution of the mean toroidal (upper) and poloidal (lower) magnetic fields for case A. Each sample involves azimuthal averages, accompanied by a 100 days temporal average (centered about the indicated times). Helical structures of opposite polarity wax and wane over the course of the 17,000 days sampled. Magnetic field strength is shown in color; contours indicate poloidal field lines for $B_{\rm pol}$, and zero field strength for B_ϕ (units in kG).

(A color version of this figure is available in the online journal.)

mean toroidal and poloidal magnetic fields for the greater part of the overall evolution. Two prominent twisted structures of opposite helicity have developed near the equator for our mixed case. Both torii persist on timescales of order the diffusion time, but the northern, negatively signed torus tends to vary in strength more than its southern counterpart, disappearing completely after about day 10,000. These oppositely signed toroidal tubes with a common, enveloping poloidal component have typical field strengths of a few tens of kG, with peak mean field strengths of around 100 kG near their centers. For comparison, overall peak field strengths of 350 kG are achieved within the core. Evolution of the system for multiple diffusion times leads to the emergence of a single positively signed toroidal flux structure in the radiative envelope.

The prominent equatorial torii that develop mainly in the radiative exterior at low latitudes reside in a region previously characterized by strong rotational shear. The energy initially in the differential rotation (DRKE) is insufficient to account for the bulk of the magnetic toroidal energy (MTE) contained in these structures, since the DRKE comprised only about 10% of the total KE initially. Values of MTE near the end of the simulation (then comparable with KE) are roughly five times the initial value of DRKE. Rather than reflecting field structures that truly encircle the convective core, the torii of Figure 9 represent the mean of a more complicated magnetic geometry as seen in Figure 7. Thus while an Ω-effect is certainly at work on the poloidal fields in this region, nonaxisymmetric motions are responsible for the bulk of the mean field generation here. We discuss these generation mechanisms further in Section 10.

7. NATURE OF DIFFERENTIAL ROTATION

The coupling of convection with rotation tends to redistribute angular momentum so that differential rotation is established, yet the structure and amplitude of such rotational shearing flows is difficult to predict. Browning et al. (2004) explored the differential rotation established by core convection in the purely hydrodynamic version of our A-type star. The convection yields a slow column of differential rotation throughout the core. With the inclusion of magnetism, and the realization of dynamo activity as in case C4m, this differential rotation is considerably weakened, but the slowly rotating (retrograde) central column of fluid (Figure 1(d)) is retained. The radiative zone close to the equator exhibits a prograde mean zonal flow $\langle v_\phi \rangle$.

Imposing mixed or poloidal external magnetic fields alters the differential rotation until the radiative zone is nearly in solid body rotation (Figures 10(a) and (b)). The slow central column of retrograde flow in the progenitor case is largely absent, replaced by a region of slightly prograde rotation close to the rotation axis. Magnetic torquing resulting from correlations between the imposed poloidal field and the subsequently developing toroidal fields transports much of the angular momentum from the radiative zone (seen as the faster v_ϕ in Figure 1(d)) into the convective core. Radial and latitudinal shear throughout much of the domain is diminished at late times, particularly near the core and radiative zone interface. A weak retrograde jet has formed coincident with the location of the large helical magnetic structures (evident in B_ϕ in Figure 9) formed close to the interface. The super-equipartition state arising from the imposition of a mixed magnetic field has thus significantly diminished the differential rotation present in the progenitor case.

Weak departures from solid body rotation in the outer radiative envelope of case A are generally columnar in nature, with lines of constant Ω cutting across field lines in the radiative envelope. There the angular momentum transport is dominated by magnetic torques and meridional circulations. Magnetic

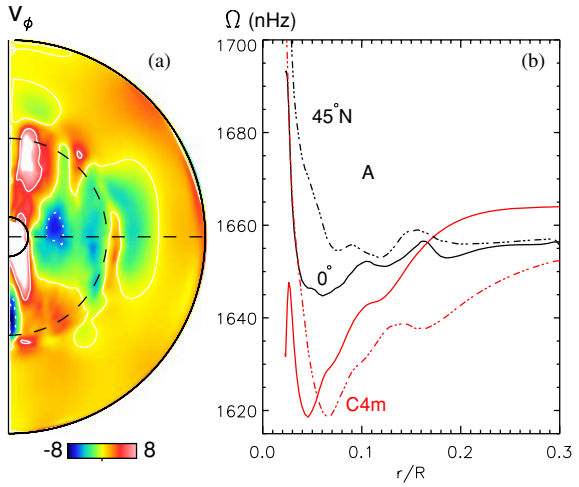

Figure 10. Differential rotation realized in case A. (a) Zonal velocity v_ϕ averaged over longitude and over 200 days around day 15,000. (b) Radial cuts of mean angular velocity Ω at low (0°) and mid latitudes (45°N) for case A (black) and case C4m (red). The radiative zone is in a state of near solid body rotation for case A. The system frame rate Ω_0 is 1655 nHz.

(A color version of this figure is available in the online journal.)

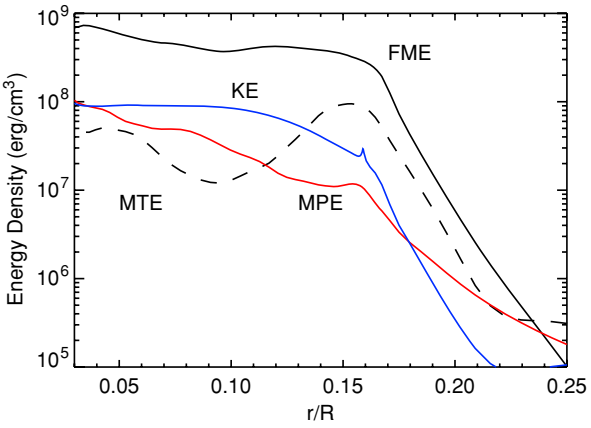

Figure 11. Variation with proportional radius of horizontally averaged kinetic and magnetic energy densities for case A. Profiles are averaged over 100 days near day 15,000. The penetrative convective core boundary is roughly at $r = 0.16R$.

(A color version of this figure is available in the online journal.)

torques realized in case A are much stronger relative to case C4m owing to the large axisymmetric fields realized in the radiative envelope of case A. However, transport of angular momentum by meridional circulations prevents a pure state of isorotation as suggested by Ferraro's law (Ferraro 1937) along magnetic field lines, ultimately maintaining a differential rotation similar in nature (but weaker in amplitude) to that achieved primarily through meridional circulations and viscous transport in the progenitor case C4m.

8. DISTRIBUTION OF MAGNETIC ENERGY

Magnetic energy in case A is largely contained within the convective core of the A-type star. However, convective overshoot, meridional circulations, and diffusion serve to transport some magnetic field into the overlying radiative zone. We now examine several components of the magnetic energy and their distribution throughout the computational domain. Various time-averaged magnetic and kinetic energy densities are shown as a function of radius in Figure 11. These quantities have been averaged over the full sphere at each radius and then temporally averaged over the interval spanning 15,000–15,100 days. Magnetic fields are super-equipartition compared to the kinetic energy throughout the core and the region of overshooting owing largely to fluctuating magnetic fields (FME). The mean field energies MTE and MPE are largely sub-equipartition throughout the core. However, the mean toroidal fields peak to super-equipartition values near the interface, owing to the development of large toroidal bands of the magnetic field there. Magnetic energies of all types fall off substantially outside of $r \sim 0.16R$, the approximate outer edge of the region of overshooting. Magnetic energies in the remainder of the radiative zone are achieved largely through diffusive processes. The energy balance both inside and outside the core is detailed in Table 1. All energies are quoted relative to the average KE in each region.

Table 1
Magnetic-to-Kinetic Energy Ratios

Region	Convective Core	Radiative Envelope
ME/KE	7.38	5.18
FME/KE	6.36	3.75
MTE/KE	0.64	1.22
MPE/KE	0.38	0.21

Notes. Time- and volume-averaged magnetic energies compared to KE. Temporal averaging covers days 15,000–15,100 as in Figure 11. Volume averaging is carried out over the convective core ($r \leqslant 0.15R$) and over the radiative envelope ($r > 0.15R$).

9. GROWTH OF LARGE-SCALE MAGNETIC STRUCTURE

The addition of our fossil field has led to the development of larger-scale magnetic structures than those present in the progenitor simulation. Figure 12(a) depicts the time-averaged magnetic energy spectrum (with spherical harmonic degree ℓ) soon after the imposition of an external field in case A. Shown also is the spectrum for a more mature stage ($\sim$ day 15,000) during the simulation after super-equipartition magnetic fields have developed. Individual spectra were created using spherical shells at mid-core and averaged over about 200 days in each case. Magnetic energy has increased on scales as small as spherical harmonic degree $\ell = 60$, but the larger scales ($\ell \leqslant 10$) exhibit the most growth. The mixed external field has thus led to the growth of the large-scale components of the magnetic field, while leaving the energy in the smaller structures relatively unchanged. Moreover, these structures are largely nonaxisymmetric, with axisymmetric structures comprising only about 20% of the magnetic energy on average.

The accompanying kinetic energy spectra are shown in Figure 12(b). As the dynamo reaches super-equipartition levels, kinetic energy decreases by a factor of about 2 across much of the spectrum. This trend reflects the overall decrease of kinetic energy shown in Figure 3 and the transition of the system to a less turbulent state.

The growth of a large-scale magnetic structure is also apparent in volume renderings of the magnetic energy in Figure 13, showing snapshots of the ME just prior to inserting the external field and during the super-equipartition phase (day 15,000). The rendering of the full convective core conveys a good sense of the helical convection in the core. The ribbons of magnetic energy seen at early times (Figure 13(c)) have become noticeably wider in the super-equipartition regime (Figure 13(d)). Similar

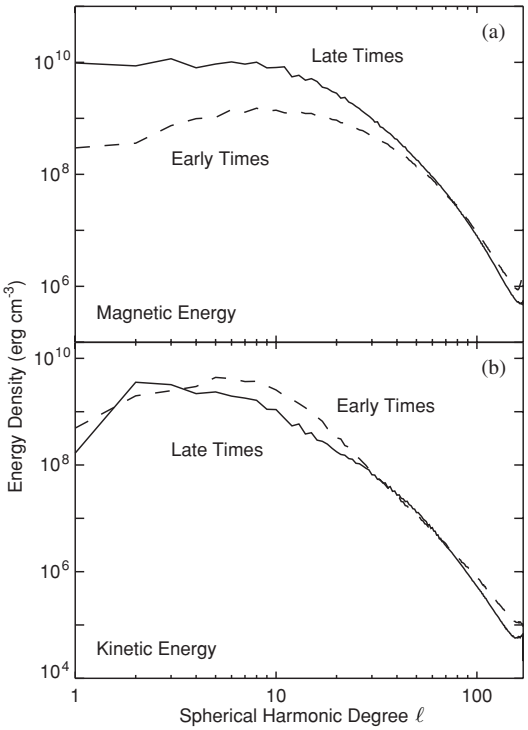

Figure 12. Magnetic and kinetic energy spectra sampled at mid-core in case A for early and late times. (a) Time-averaged initial ME spectrum (dashed line) and the spectrum realized after 15,000 days (solid line). (b) Accompanying KE spectra. The imposition of mixed fields in case A has yielded a dynamo with more prominent global-scale magnetic fields than in progenitor case C4m.

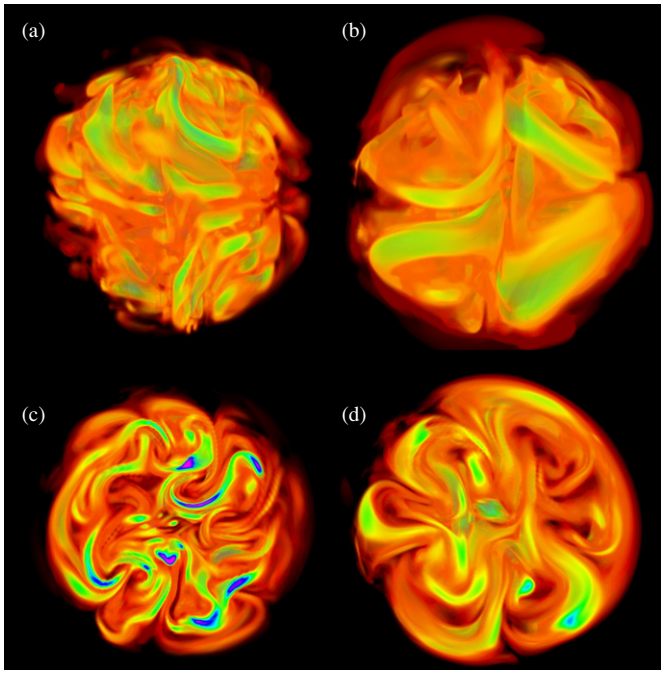

Figure 13. Volume rendering of magnetic energy density viewing the entire convection zone (a) prior to the insertion of the fossil field, and (b) 15,000 days later. The rotation axis is vertical. Structures are noticeably larger in scale in the later super-equipartition regime. Companion images of magnetic energy density viewing the equatorial plane from the north, showing (c) progenitor state and (d) mature super-equipartition state.

(A color version of this figure is available in the online journal.)

morphology is apparent in renderings of ME in the equatorial plane. The early time (Figure 13(c)) exhibits much smaller-scale fields than the later time (Figure 13(d)). The shift in peaks of KE and ME in the energy spectra of Figure 12 suggests that the dynamo now running in case A is much more global scale in nature than that in the progenitor case C4m.

10. SUSTAINING A SUPER-EQUIPARTITION STATE

The super-equipartition state achieved here in which magnetic energy is 10-fold greater than the convective kinetic energy is quite remarkable, for one might anticipate that the feedback from the Lorentz forces would prevent this. In contrast, the progenitor case C4m was nearly in equipartition by this measure. So how does case A achieve and sustain such strong magnetic fields? The shift toward larger-scale convective motions and magnetic field structures suggests that a more global field/flow topology is necessary for this state. The high magnetic field strengths realized in case A might be anticipated to yield Lorentz forces that react back on the flow, ultimately quenching the flows that generate such fields through an α-quenching process (Cattaneo & Hughes 1996). For our energy balance to survive, the flows must organize themselves in a fashion that minimizes these Lorentz forces while still maintaining sufficient induction to balance the dissipative processes present in the system (which also serves here to provide some field reconnection). This may be accomplished by separating regions of strong flow from those of the strong magnetic field, or by some tendency to align $\boldsymbol{j}$ and $\boldsymbol{B}$ and thereby lessen Lorentz force feedbacks. We turn now to a discussion of these issues and of the dominant mechanisms responsible for magnetic field generation in case A.

10.1. Surviving Lorentz Feedbacks

We can assess the nature of alignment and displacement of the field and flow by examining their large-scale organization as illustrated in Figure 14. Here instantaneous snapshots of magnetic energy and kinetic energy near day 15,000 are overlaid at two depths and in an equatorial cut. Regions of strong ME are shown in blue, strong KE in red, and regions where both are strong (relative to their rms values) are shown in green. Clearly the patterns in KE are similar to those seen in ME. However, some of the features are laterally displaced, with arcs of ME running adjacent to arcs of KE. Some patches of overlap are visible as well, particularly in Figure 14(c) which suggest that some strong magnetic structures merge with fast velocity structures. For such overlapping regions to survive, Lorentz forces must not be strong enough locally to disrupt the flow. This, in turn, implies some alignment of $\boldsymbol{j}$ and $\boldsymbol{B}$. The current density $\boldsymbol{j}$ depends, through Ohm's law, on both the electric field and on the alignment of flows and fields (through $\boldsymbol{v} \times \boldsymbol{B}$). Minimizing the Lorentz force locally thus typically implies some alignment of $\boldsymbol{v}$ and $\boldsymbol{B}$.

The large-scale alignment of flows and fields may be explored through volume renderings as in Figure 15(a) where instantaneous streamlines are depicted in the equatorial region. The corresponding ME (Figure 15(b)) and a combined rendering of these two quantities (Figure 15(c)) are illustrated as well. The large, cloverleaf-type patterns in the ME are typically tangent to the local magnetic field vector. Rendered in the same image, the two patterns trace each other closely, with alignment most evident in regions of the strong magnetic field. Another measure of the alignment of flows and magnetic fields is achieved by examining the relative angle θ between $\boldsymbol{v}$ and $\boldsymbol{B}$ throughout the core. Figure 16, examining pdf's of that angle, shows that our

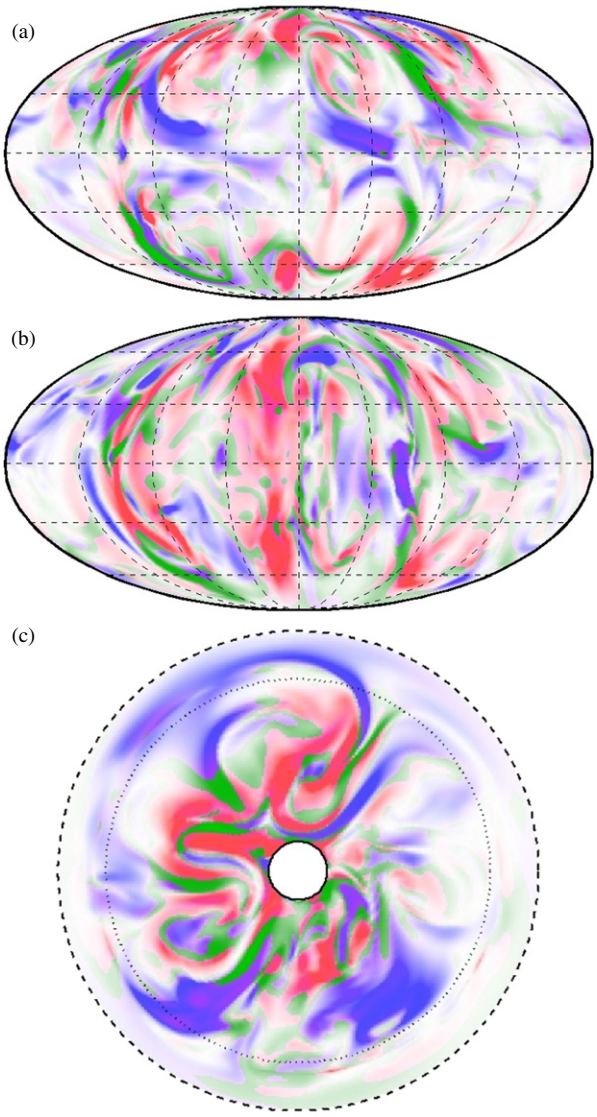

Figure 14. Dual rendering of KE (red) and ME (blue) near day 15,000. Regions where both quantities are strong (relative to their respective rms values) appear in green. (a) Mollweide view at the interface between the core and the radiative zone ($r = 0.15R$), and (b) at mid-core ($r = 0.075R$). (c) Partial view of the equatorial plane from the pole. The dotted line denotes the edge of the convective core, and the outer dashed line $r = 0.19R$, capturing a portion of the radiative zone (including the region of overshooting).

(A color version of this figure is available in the online journal.)

evolved case A typically exhibits more alignment than the progenitor case C4m. By weighting these by the local KE and ME, thus concentrating on regions of fast flow and the strong field, the alignment becomes more pronounced. This may be seen by forming pdf's where both $\boldsymbol{v}$ and $\boldsymbol{B}$ exceed a threshold of either just their rms values (curve A1) or twice those values (A2). For the latter, the pdf peaks at $\theta \sim 10^\circ$, compared to sampling all sites which yields a broad maximum centered on 25°.

10.2. Global Connectivity of Structures

Figure 15 showing an equatorial cut has emphasized that the core is typically occupied by 4–6 cylindrical convective rolls, with their axes primarily aligned with the rotation axis, as suggested by Figure 5(d). The geometry and connectivity of the flows in this system play a significant role in how the strong magnetic fields are built and sustained. Turning to analysis of flow streamlines shown variously in Figure 17, we see that the rolls typically possess a narrow core, with a prominent upward or downward velocity (say v_z) along the rotation axis. Within each roll, surrounding the fast core is a broader region of circular flow in a plane nearly perpendicular to the rotation axis. As these convective motions overshoot into the radiative zone, buoyancy forces brake the radial component of the flow. The resulting tilt of the roll motions reflects the slope of the intersection of the roll with the edge of the convection zone and is similar to that observed in simulations of rotating spherical shells with rigid boundaries (e.g., Busse 2002). These outer regions of the rolls exhibit a weaker v_z than in the fast core of the roll, though of the same sense, thus yielding helical flow lines.

It is quite striking that the fast axial core flow in one roll can often be seen to connect near the radiative interface to the core flow (of the opposite sense) in an adjacent roll. The axial core flows extend along with the overall roll structure across the equator, though there are some examples in which the sense of the axial flow changes at the equator. These axial core flows can thus serve to effectively connect the two hemispheres, in addition to linking neighboring rolls.

The coupling of the rolls is also evident in the time sampling of both streamlines and ME shown in equatorial cuts in Figure 18. Close study shows that there are frequent events in which streaming flows extend across the full domain, thereby coupling opposite sides of the convective core. It appears that the genesis of such streaming flows comes from two counter-rotating rolls on one side of the convective core (yielding a zone of converging flow toward the rotating axis) becoming correctly phased with another set of rolls on the opposite side that are driving some flow away from the axis. Such large-scale flows appear to be crucial to establishing the largest magnetic structures built by the dynamo action. As these streaming flows couple distant portions of the core, they stretch and advect the fields into the configurations seen in the evolving ME patterns. Figure 18 shows that broad swathes of the magnetic field extending across the convective core are nearly coincident with the fast core crossing flows. Thus it appears that attaining a global-scale magnetic field within a core that possesses little differential rotation, yet senses Coriolis forces significantly, relies on the large-scale connectivity among the evolving system of rolls.

Although the convective rolls are fairly complex and variable in time, the more prominent rolls maintain their coherence for a few tens of rotation periods. The prominent axis-crossing motions serve to connect rolls on opposite sides of the core, stretching the magnetic field from one roll to another as they do so. The resulting magnetic field structures thus thread through multiple rolls, connecting across the rotation axis and along the periphery of neighboring cells. The topology has thus become much more global in scale, resulting in the notable spectral change seen in Figure 12.

10.3. Details of Magnetic Field Generation

As the magnetic energy in case A is manifest predominantly in the fluctuating (nonaxisymmetric) magnetic fields, we focus on the generation of FME here. The generation of energy in the fluctuating fields may be computed by taking the dot product of the induction equation with the fluctuating magnetic field $\boldsymbol{B}'$. Contributions to the generation of FME arise from correlations between fluctuating flows and fields with both their fluctuating and mean counterparts. However, while mean flows and magnetic fields contribute to the generation and destruction of FME, we find that the primary balance is struck between

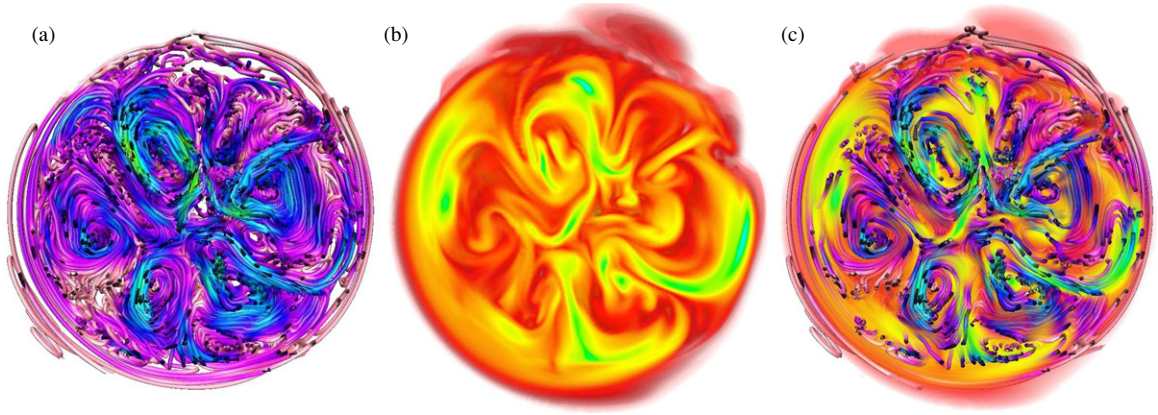

Figure 15. Comparing partitioning of fast flows and strong fields in a snapshot sampled in the equatorial region. (a) Instantaneous flow tangent lines (day 9000). Coloring in blue/green indicates the fastest speeds (∼30 m s^{-1}) and regions of violet/pink that of weaker flows (∼5 m s^{-1}). Six prominent rolls are present. (b) Patterns of stronger magnetic energy are similar to those of the faster flows though somewhat displaced. Regions of bright green denote ∼250 kG fields, reddish regions ∼30 kG fields. (c) Flow lines and ME rendered together. Regions of fast flow and strong fields exhibit notable alignment.

(A color version of this figure is available in the online journal.)

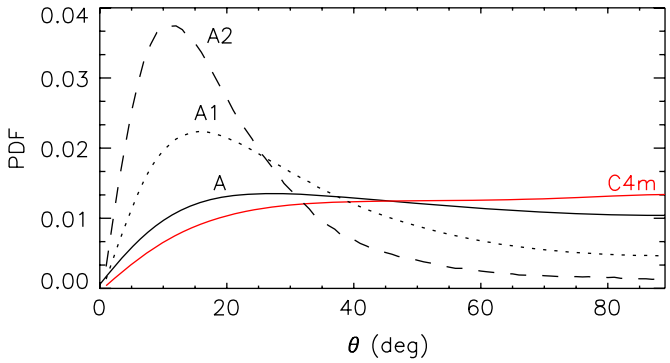

Figure 16. Probability distribution functions of the relative angle θ between $\boldsymbol{v}$ and $\boldsymbol{B}$ measured throughout the convective core for cases A (black) and C4m (red), averaged over about 50 realizations spanning 100 days. Flows and magnetic fields exhibit more alignment in the super-equipartition regime of case A than in case C4m. The alignment of flow and magnetic fields in case A is more pronounced in regions of strong flow and field, shown by plotting pdf's only for sites where local values of both $\boldsymbol{v}$ and $\boldsymbol{B}$ exceed their rms values (labeled A1) or twice those values (A2).

(A color version of this figure is available in the online journal.)

terms involving shearing, diffusion, and advection associated with the fluctuating components of the flow and magnetic field so that

$$\frac{\partial(\mathrm{FME})}{\partial t} \approx 0 \approx \frac{1}{4\pi}\boldsymbol{B}' \cdot [\underbrace{(\boldsymbol{B}' \cdot \nabla)\boldsymbol{v}'}_{\text{shearing}} \underbrace{-\nabla \times (\eta \nabla \times \boldsymbol{B}')}_{\text{diffusion}} \underbrace{-(\boldsymbol{v}' \cdot \nabla)\boldsymbol{B}'}_{\text{advection}}] \quad (20)$$

holds approximately. We examine the contributions of these individual terms to the generation and dissipation of the constituents of FME (namely FPE and FTE) in Figure 19.

The local enhancement and diminishment of FPE by advection (Figure 19(a)) reflect the columnar nature of the rolls. Orbital motions about the axes of these rolls efficiently carry FPE from regions of generation (via shearing as in Figure 19(b)) to the rest of the core. Generation of FPE occurs primarily near the rotation axis and near the outer boundary of the core. The noticeably weak columnar region of generation at mid-core is roughly coincident with the location of the roll axes. Orbital motions of the rolls are largely parallel to the equatorial plane throughout most of the core. As buoyancy brakes the radial component of these motions in the region of overshooting, the resulting motions tend to conform to the spherical boundary of the core. The ensuing tilting of the orbits (see Figure 17) sets up a region of shear between the rotation axis and the outer core that serves to generate a field parallel to the core boundary. Additional generation of magnetic field in the outer core also occurs through shearing in the azimuthal direction that serves to convert B_ϕ into B_r and B_θ there. Generation of FPE near the rotation axis, somewhat stronger than that seen in the outer core, is accomplished primarily through generation of B_r due to shearing of B_ϕ. The close proximity of inflows and outflows of the columnar rolls near the rotation axis sets up regions of strong shearing of radial flows (see Figures 18(a) and (c)) that efficiently stretches the strong azimuthal field generated in this region into a radial field. Core-crossing flows in particular, such as that prominently visible in Figure 18(d), have a similar effect in this region.

The effect of advection on FTE (Figure 19(d)) is similar to that seen with FPE in that circulations generally carry energy away from the region of strong generation near the rotation axis (Figure 19(e)) to the outer core where less generation occurs. Generation of FTE occurs primarily near the rotation axis as well. The convergence of multiple rolls at the rotation axis sets up gradients of v_ϕ in the direction perpendicular to the rotation axis, resulting in strong shear in this region. Moreover, core-crossing motions such as in Figure 18(d) will effectively shear the radial field orthogonal to these motions, generating an azimuthal field in the process. An additional effect, not included in the decomposition of Figure 19, is the action of mean shear near the rotation axis (see Figure 10(a)) acting on the nonaxisymmetric B_r and B_ϕ. Very near the rotation axis, the generation of FTE through this shearing effect is comparable to that due to the nonaxisymmetric flows. We note that no similarly strong effects of mean flows on generation of FPE is observed. An additional region of strong generation of FTE is present at the outer boundary of the convective core. In contrast to FPE, the geometry of this region is largely spherical in nature owing to the transition from relatively strong azimuthal flows in the core to a region of nearly solid body rotation in the radiative zone.

The effects of diffusion on FPE and FTE (Figures 19(c) and (f)) are strongest near the rotation axis and weakest in the outer core where advection mitigates the effects of generation

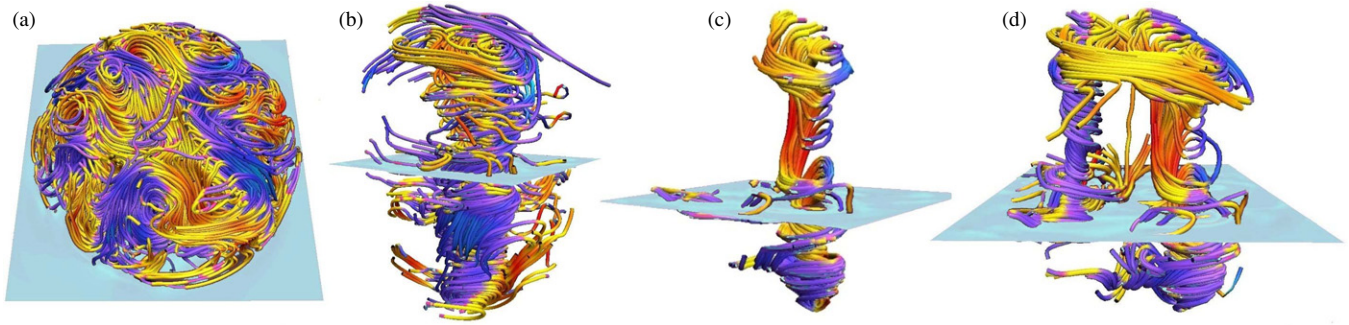

Figure 17. Columnar convection for case A visualized using instantaneous streamlines near day 15,000. Streamlines are colored by the velocity component along the rotation axis v_z. Blue (yellow) tones indicate northward (southward) motion; the equatorial plane indicated by light blue. (a) View of convective core from the north. The core is typically dominated by 4–6 prominent rolls. (b) Individual columnar cell from the roll complex. The columnar motion extends across the equatorial plane. Tilting of the orbits due to the spherical boundary of the core is visible. (c) Interior view of the same roll. Many rolls in this system possess an axial flow. Such flows freely cross the equatorial plane as seen here. (d) Rendering of that roll along with a neighboring roll. Axial flows tend to link neighboring rolls near the edge of the convective core.

(A color version of this figure is available in the online journal.)

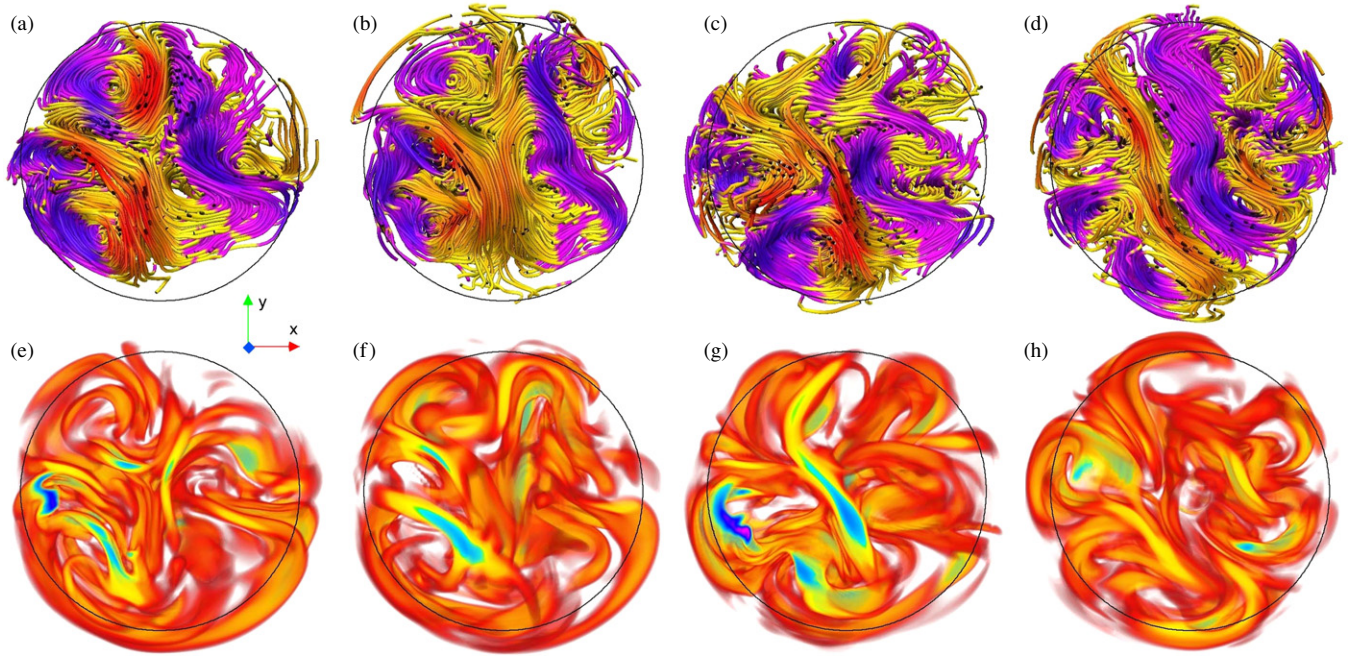

Figure 18. Sampling the evolving flow streamlines (a)–(d) and accompanying ME (e)–(h) close to the equatorial plane in four time instants each separated by about 50 days (starting at day 9000). Violet tones indicate positive motions in the y-direction, and yellow tones negative motions. Regions of strong ME are shown in yellow/green tones.

(A color version of this figure is available in the online journal.)

more readily. The net effects of diffusion in the regions of generation is thus to destroy FTE and FPE. Beyond the region of overshooting, however, diffusive processes serve to carry energy from the outer edge of the convective core into the radiative zone where generation of a magnetic field is minimal.

11. MULTIPOLAR EXTERNAL FIELDS

We have thus far investigated the effects of an external field involving only a dipolar ($\ell = 1$) magnetic field. However, measurements of magnetic fields in Ap stars suggest that the surface fields of these stars involve multipolar components with spherical harmonic degrees greater than $\ell = 1$. It is appropriate to examine the effects of more complex magnetic topologies on the system. Does the scale of the imposed magnetic flux matter, and if so, how? We have thus examined two additional external field configurations, with $\ell = 2, m = 0$, and $\ell = 4, m = 0$. In each case, the strength of the fossil field was adjusted so that the integrated unsigned magnetic flux across the convective core boundary was identical to that in the mixed-field case A. Unlike the mixed-field case, neither of these two cases possessed a net flux of the magnetic field through either hemisphere. Moreover, here there was no magnetic flux linking the northern and southern hemispheres of the star across the equator.

We show the evolution of the energies for these two cases in Figure 20. In each, a transition to super-equipartition is evident. However, the growth of the $\ell = 2$ case (Figure 20(a)) is faster than that of the $\ell = 4$ case (Figure 20(b)). Each of these exhibit growth that is in turn slower than the dipolar cases. The mechanisms that cause the growth clearly have a dependence on length scale. Magnetic energy spectra for these cases (Figure 20(c)) are qualitatively similar to those of the mature mixed-field case A. In both instances, larger-scale fields have grown more than the smaller-scale fields.

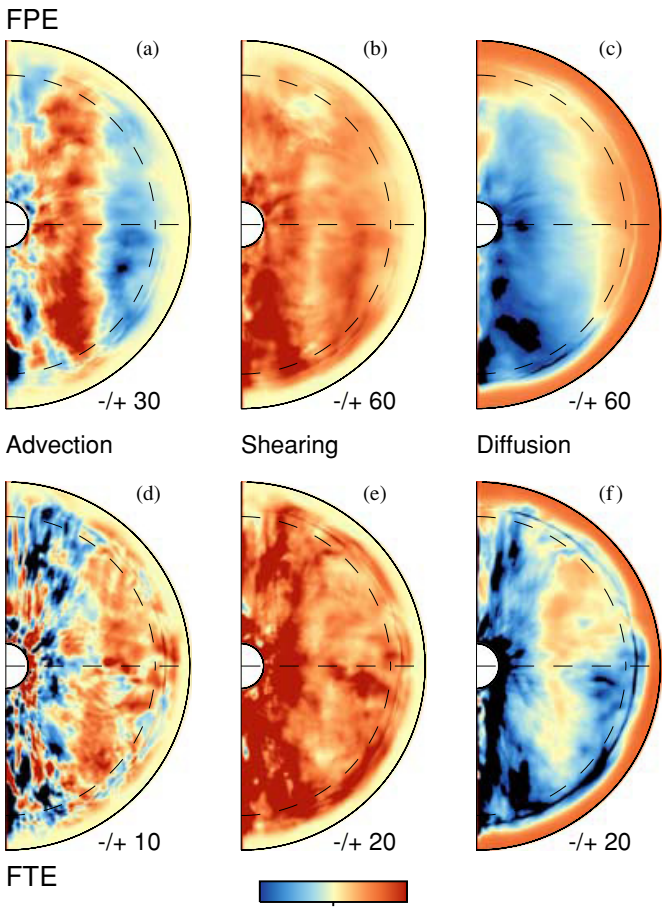

Figure 19. Generation and dissipation of fluctuating magnetic energy for case A. Top row: generation of FPE from (a) advection, (b) shearing, and (c) diffusion. Bottom row: generation of FTE likewise from (d) advection, (e) shearing, and (f) diffusion. Generation terms are shown in erg cm^{-3} s^{-1} and have been averaged in azimuth and in time over 200 days near day 15,000.

(A color version of this figure is available in the online journal.)

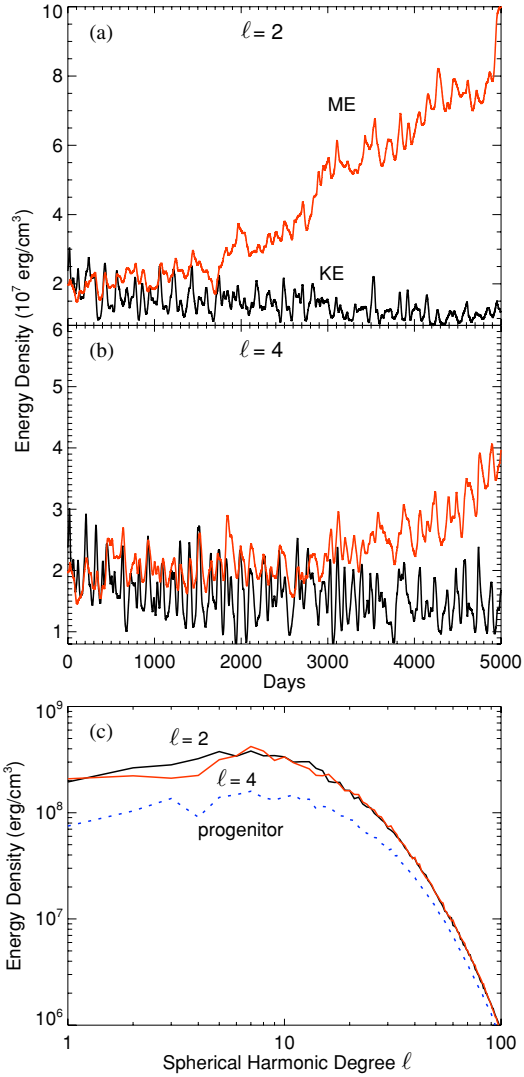

Figure 20. Multipolar cases. (a) Temporal evolution of the quadrupolar $\ell = 2$ case. Volume-averaged ME is shown in red and KE in black. (b) Evolution for the $\ell = 4$ multipolar case. (c) Spectra at mid-core for both cases at day 4000. $\ell = 2$ is shown in black and $\ell = 4$ in red. The progenitor case is shown in blue (dotted) for reference.

(A color version of this figure is available in the online journal.)

Evolution of the axisymmetric fields for the $\ell = 2$ and $\ell = 4$ cases are shown in Figures 21 and 22, respectively. The effects of weak differential rotation (Ω-effect) initially operating in the radiative zone are evident in snapshots of the toroidal fields. Such banded toroidal structures give way to those produced by processes in the core as the initial poloidal field component diffuses away and the differential rotation subsides. In each case, the imposed magnetic flux is reprocessed by the core until a roughly dipolar field configuration is realized within the core. Continued pumping of this field into the radiative zone, combined with diffusion of the imposed fossil field placed there, leads ultimately to a magnetic field geometry which is largely dipolar in the radiative zone in both cases. This behavior suggests that the linkage of the initial fossil field to that inside the core is not crucial to achieving a super-equipartition state. Rather, it seems that the scale over which magnetic field lines are able to connect distant regions of the core may be key.

12. CONCLUSIONS AND PERSPECTIVES

Our work has revealed that a remnant primordial field linking the convective core and the radiative envelope of an A-type star may significantly impact the dynamics of convection within the core. By placing a modest fossil field into the radiative zone involving a 10% increase in the total magnetic energy, the dynamo responds by a fivefold increase in the overall magnetic energy in the system. With an accompanying twofold decrease in convective kinetic energy, the dynamo is now in a super-equipartition state with the ratio of ME/KE of order 10. The bulk of the magnetic energy (about 85%) achieved through the resulting dynamo action is contained in the fluctuating (nonaxisymmetric) magnetic fields, with about 10% in mean (axisymmetric) toroidal fields and about 5% of the energy contained in the mean poloidal fields.

The mean magnetic fields built in this regime are substantial, with peak mean toroidal field strengths of around 10^5 G (about one-third of the peak fluctuating fields found in the core). The mean toroidal fields typically manifest as large, oppositely signed torii encircling the convective core just above and below the equatorial plane. These bands wax and wane in strength over time, but maintain their approximate antisymmetry about the equatorial plane. The mean poloidal fields in case A exhibit a prominent dipolar component with strengths of around 2×10^4 G near the edge of the core. While the strength of the poloidal field is variable in time, we have observed no flip of the dipole

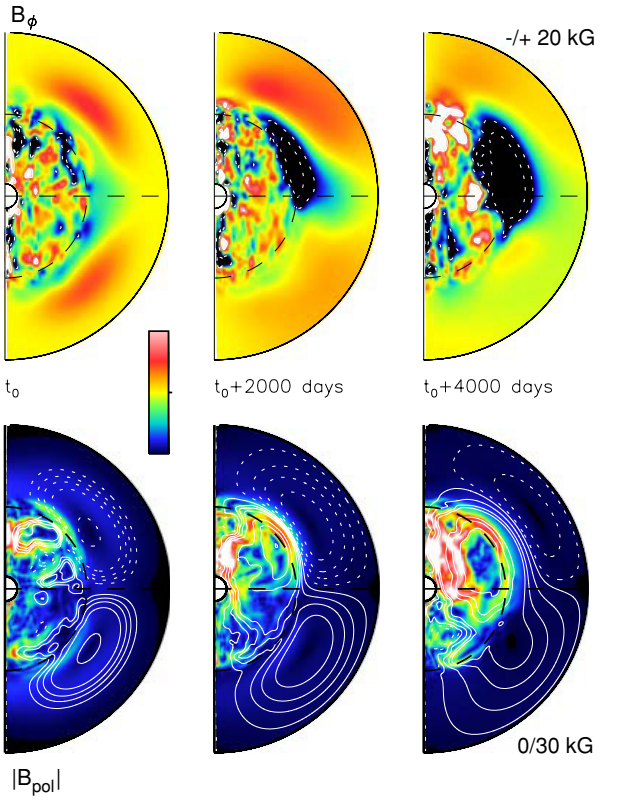

Figure 21. Mean field evolution for the quadrupolar $\ell = 2$ case. Upper row: azimuthally averaged B_ϕ at three instants in time spanning 4000 days. Lower row: corresponding mean poloidal fields. White lines denote poloidal field lines. Solid lines are counterclockwise, and dashed lines are clockwise. The colored underlay indicates the strength of the mean poloidal field modulus.

(A color version of this figure is available in the online journal.)

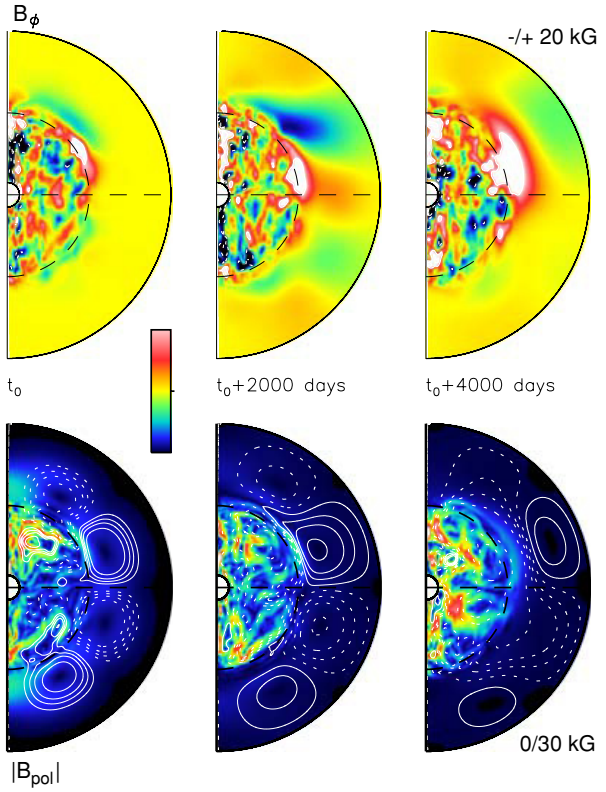

Figure 22. As in Figure 21 showing the $\ell = 4$ multipolar case. Upper row: azimuthally averaged B_ϕ at three instants in time spanning 4000 days. Lower row: corresponding mean poloidal fields. Magnetic fields in the $\ell = 4$ case also evolve toward a dipole in the radiative zone.

(A color version of this figure is available in the online journal.)

moment in the roughly three magnetic diffusion times spanned by the simulation.

We have examined the sensitivity of the super-equipartition transition to the structure of the imposed mean field as well. Toroidal external fields with some threading through the core have no effect. Rather, the transition requires an external field with a poloidal component. Systems with smaller-scale poloidal fields ($\ell = 2$ and $\ell = 4$) take longer for a transition to occur but reach end states similar to case A and case B ($\ell = 1$). All of these systems are characterized by super-equipartition between the magnetic and kinetic energy, diminished differential rotation throughout the core, and a tendency to develop a mean poloidal field configuration that is dipolar in nature. The sign of the dipole moment for the $\ell = 2$ case is the same as that of case A, but that for the $\ell = 4$ case is oppositely directed, suggesting that the external field may bias the system in some fashion.

12.1. Sustaining the Strong-field Dynamo

The maintenance of such strong magnetic fields is an intricate matter, particularly in light of the strong Lorentz forces that potentially accompany them. Organization of flows in a fashion that minimizes Lorentz feedbacks is thus crucial to this balance. The velocity configuration in case A is characterized by 4–6 prominent convective rolls aligned with and extending along the rotation axis. Convective motions in these rolls are largely perpendicular to the rotation axis except in the roll center. There pressure gradients induced by tilting of the roll orbits at the spherical boundary of the convective core induce flows along the roll axis. Some of these axial flows originate and terminate at the equatorial plane, while others flow freely between the two hemispheres (Figure 17). The substantial reduction in differential rotation in this system has allowed for axis crossing streaming flows. When rolls phase properly, inflow (i.e., toward the rotation axis) from one roll may cross the rotation axis, merging with the outflow of another roll.

The convective state achieved in case A thus exhibits motions that are much more global in nature (Figure 12) than case C4m, and the core is in general more topologically connected as a result, particularly through the intermittent core-crossing motions. The magnetic fields of case A follow a similar trend, exhibiting a much more global-scale field topology than in case C4m. Magnetic structures typically wrap around the boundaries of the convective columns in large arching helical bands of the field. Moreover, core crossing flows display a clear magnetic signature (Figure 18), with large bundles of magnetic flux stretching across the core, linking rolls on opposite sides of the core.

We find that the coexistence of our convection with these strong magnetic fields relies on a greater co-alignment of the flows and magnetic fields than that achieved in case C4m. Magnetic field structures tend to mimic patterns visible in streamline renditions of the flow field, suggestive of a guiding effect of the magnetic field on the flow. However, regions of the strong field are typically separate from (albeit often adjacent to) regions of strong flow. This is particularly true of the fast axial flows in the center of the convective columns. We find these regions to be largely devoid of magnetic energy.

Our primary case A bears some similarities to phenomena observed in geodynamo modeling. In the absence of magnetic fields, convection in those models also exhibits a strong tendency for Taylor columns aligned with the rotation axis (e.g., Roberts & Glatzmaier 2000). As with our case A, the convection within their cells is helical, with axial flows setting up circulations linking neighboring columns at high latitudes and near the equatorial plane. In the presence of magnetism, this convection maintains its columnar nature, and the associated helical motion serves to create an efficient α-effect as the magnetic field is stretched and twisted around the convective rolls (e.g., Olson et al. 1999). Super-equipartition is found in these models as well, with typical values of ME/KE of 10–20, but with some reaching as high as 10^3 (Kuang & Bloxham 1999; Glatzmaier et al. 1999). This regime, referred to as the strong-field regime, involves comparable Lorentz and Coriolis forces. As the inner 35% of the Earth's core is solid, geodynamo models have an inner sphere that flows may not cross. Dynamics closer to the rotation axis than the tangent cylinder associated with this inner sphere can be considerably different than that occurring within the outer convective rolls. Olson et al. (1999), for example, noted the presence of thermally driven upwellings along the rotation axis in the tangent cylinder that tend to modify the mean poloidal field, effectively lowering the poloidal flux through the core boundary at the poles. We observe no such effects in our A star simulations as the tangent cylinder is much less pronounced, with flows crossing the rotation axis freely above and below our small inner cutout.

The force balance achieved in geodynamo models typically involves some balance between the Lorentz, Coriolis, and buoyancy forces (Christensen & Aubert 2006). Such a force balance was not present in the progenitor C4m which was largely geostrophic in nature. However, the super-equipartition state realized in case A does exhibit such a triple force balance in the direction parallel to the rotation axis. Pressure plays a stronger role in the horizontal, where the predominant balance is between pressure, Coriolis, and Lorentz forces.

Inertial forces are weak in geodynamo models. Due to the rapid rotation of the Earth and the relatively weak convective velocities achieved, geodynamo models are much more rotationally constrained than our A star models. A typical Rossby number, which measures the inertial force relative to the Coriolis force, is about 10^{-5} in the geodynamo versus about 10^{-3} for our A star. We find the inertial term in case A, while diminished relative to the progenitor case C4m, to be non-negligible in our simulations, typically contributing to the force balance at the 10% level.

Saturation in geodynamo models can involve the advection (driven by the axial circulations within the rolls) of the poloidal field into the centers of anticyclonic rolls. Equilibration between Lorentz and Coriolis forces is achieved in these rolls through an outward directed Lorentz force that counteracts the inward Coriolis force (Sakuraba & Kono 1999; Olson et al. 1999), a phenomenon that we do not observe in our super-equipartition cases. Instead for our case A, the magnetic fields exhibit a tendency to encircle the rolls, leaving the roll centers relatively devoid of a magnetic field. The encircling field has the net effect of squeezing individual rolls. For a given intersection of two rolls pervaded by magnetic flux, Lorentz forces may work in tandem with the Coriolis force on one side of the intersection and against it on the other. The similarities of our super-equipartition dynamos to the geodynamo are nevertheless striking. It seems that by imposing a modest external field we have enabled our system to transition toward the strong-field dynamo regime.

12.2. Possible Field Emergence

We have demonstrated that the presence of a fossil field may induce the core dynamo of an A star to transition to a more laminar but stronger dynamo state. From an observational standpoint, however, it is prudent to ask what implications such a state may have for magnetic fields at the surface. While we have not observed the rise of buoyant magnetic structures in this simulation, we do find that more efficient generation of mean fields at the edge of the convection zone has led to the development of 10^5 G fields there. Even stronger fields may be required for structures to become buoyant and eventually reach the surface, as has been considered when studying such possibilities for the more massive O and B stars (MacGregor & Cassinelli 2003; MacDonald & Mullan 2004). They suggest that fields with super-equipartition strengths would be needed to achieve field emergence. It is thus of some interest that we have found similar strong-field dynamo states for our less massive A-type stars.

We have yet to ascertain if our core dynamos have attained the upper limit for magnetic field strengths. Indeed, periods of brief super-equipartition are apparent even with the mean fields in Figure 4. What sets the strength and temporal extent of these phases is unclear, and may rely on fortuitous phasing of the convective rolls and magnetic field near the core boundary. Moreover, the development of sufficiently strong flux tubes may rely on adopting much lower diffusivities in the radiative zone, such as through hyperdiffusivity. Our eddy diffusivity parameterization for the SGS motions in this region may simply be too diffusive to allow the buildup of 10^6 G or greater fields.

Such considerations encourage detailed studies of what is required for magnetic structures to become unstable and reach the surface in these A stars. Our simulations have revealed that a distinctly super-equipartition state can be achieved by the core dynamo, yet judging from the complexities realized with geodynamos, there may well exist a wide range of strong-field states that have yet to be explored.

The authors gratefully acknowledge many helpful conversations with Mark Miesch, Benjamin Brown, and Kyle Augustson. This research is supported by NASA through Heliophysics Theory Program grants NNG05G124G and NNX08AI57G, with additional support for N.A.F. through NASA GSRP program by award NNX07AP34H. M.K.B. was supported by NSF Astronomy and Astrophysics post-doctoral fellowship AST 05-02413, and by research support now at CITA. A.S.B. was partly supported by the Programme National Soleil-Terre of CNRS/INSU (France), and by the STARS2 grant from the European Research Council. The simulations were carried out with NSF PACI support of PSC, NCSA and TACC, and by NASA HEC support at Project Columbia. Volume renderings throughout the paper were produced using VAPOR (Clyne et al. 2007).

REFERENCES

Abt, H. A. 2000, ApJ, 544, 933
Alecian, E., et al. 2008, A&A, 481, 99A
Aurière, M., et al. 2007, A&A, 475, 1053
Babcock, H. W. 1947, ApJ, 105, 105
Borra, E. F., Landstreet, J. D., & Mestel, L. 1982, ARA&A, 20, 191
Braithwaite, J. 2007, A&A, 469, 275

Braithwaite, J., & Nordlund, Å. 2006, A&A, 450, 1077
Braithwaite, J., & Spruit, H. C. 2004, Nature, 431, 819
Browning, M. K. 2008, ApJ, 676, 1262
Browning, M. K., & Basri, G. 2007, in AIP Conf. Proc. 948, Unsolved Problems in Stellar Physics, ed. R. J. Stancliffe et al. (Melville, NY: AIP), 157
Browning, M. K., Brun, A. S., & Toomre, J. 2004, ApJ, 601, 512
Brun, A. S. 2007, Astron. Nachr., 328, 1137
Brun, A. S., Browning, M. K., & Toomre, J. 2005, ApJ, 629, 461
Brun, A. S., Miesch, M. S., & Toomre, J. 2004, ApJ, 614, 1073
Brun, A. S., & Toomre, J. 2003, ApJ, 570, 865
Busse, F. H. 2002, Phys. Fluids, 14, 1301
Cattaneo, F., & Hughes, D. W. 1996, Phys. Rev. E, 54, 4534
Christensen, U. R., & Aubert, J. 2006, Geophys. J. Int., 166, 97
Clune, T. L., Elliott, J. R., Miesch, M. S., Toomre, J., & Glatzmaier, G. A. 1999, Parallel Comput., 25, 361
Clyne, J., Mininni, P., Norton, A., & Rast, M. 2007, New J. Phys., 9, 301
Cowling, T. G. 1945, MNRAS, 105, 166
Deutsch, A. J. 1956, PASP, 68, 92
Dobler, W., Stix, M., & Brandenburg, A. 2006, ApJ, 638, 336
Duez, V., & Mathis, S. 2009, Phys. Plasmas, submitted
Ferraro, V. C. A. 1937, MNRAS, 97, 458
Flowers, E., & Ruderman, M. A. 1977, ApJ, 215, 302
Freyhammer, L. M., et al. 2008, MNRAS, 389, 441
Gilman, P. A., & Glatzmaier, G. A. 1980, ApJS, 45, 335
Glatzmaier, G. A., Coe, R. S., Hongre, L., & Roberts, P. H. 1999, Nature, 401, 885
Gough, D. O. 1969, J. Atmos. Sci., 26, 448
Kochukhov, O., & Bagnulo, S. 2006, A&A, 450, 763
Kochukhov, O., et al. 2004, A&A, 414, 613
Krause, F., & Oetken, L. 1976, in Physics of Ap Stars, ed. W. W. Weiss, H. Jenkner, & H. J. Wood (Vienna: Univ. Wien), 29
Kuang, W., & Bloxham, J. 1999, J. Comput. Phys., 153, 51
Landstreet, J. D., et al. 2008, A&A, 481, 465
MacDonald, J., & Mullan, D. J. 2004, MNRAS, 348, 702
MacGregor, K. B., & Cassinelli, J. P. 2003, ApJ, 586, 480
Markey, P., & Tayler, R. J. 1973, MNRAS, 163, 77
Mathys, G. 2001, in ASP Conf. Ser. 248, Magnetic Fields Across the Hertzsprung–Russell Diagram, ed. G. Mathys, S. K. Solanki, & D. T. Wickramasinghe (San Francisco, CA: ASP), 267
Mathys, G., Hubrig, S., Landstreet, J. D., Lanz, T., & Manfroid, J. 1997, A&AS, 123, 353
Maury, A. C. 1897, Harv. Ann., 28, 96
Mestel, L. 1999, Stellar Magnetism (Oxford: Clarendon)
Miesch, M. S., Brun, A. S., DeRosa, M. L., & Toomre, J. 2008, ApJ, 673, 557
Miesch, M. S., Brun, A. S., & Toomre, J. 2006, ApJ, 641, 618
Morel, P. 1997, A&AS, 124, 597
Moss, D. L. 2004, A&A, 414, 1065
Moss, D. L. 2001, in ASP Conf. Ser. 248, Magnetic Fields Across the Hertzsprung–Russell Diagram, ed. G. Mathys, S. K. Solanki, & D. T. Wickramasinghe (San Francisco, CA: ASP), 305
Olson, P., Christensen, U., & Glatzmaier, G. A. 1999, J. Geophys. Res., 104, 10383
Prendergast, K. H. 1956, ApJ, 123, 498
Preston, G. W. 1971, PASP, 83, 571
Roberts, P. H., & Glatzmaier, G. A. 2000, Rev. Mod. Phys., 72, 1081
Royer, F., Zorec, J., & Gómez, A. E. 2007, A&A, 463, 671
Sakuraba, A., & Kono, M. 1999, Phys. Earth Planet Inter., 111, 105
Spruit, H. C. 2002, A&A, 381, 923
Stibbs, D. W. N. 1950, MNRAS, 110, 395
Tayler, R. J. 1973, MNRAS, 161, 365
Wright, A. A. E. 1973, MNRAS, 162, 339
Zahn, J.-P., Brun, A. S., & Mathis, S. 2007, A&A, 474, 145